
This is an electronic reprint of the original article.
This reprint may differ from the original in pagination and typographic detail.

Tran, Quoc; Sołowski, Wojciech Tomasz

Generalized Interpolation Material Point Method modelling of large deformation problems including strain-rate effects – Application to penetration and progressive failure problems

Published in:
Computers and Geotechnics

DOI:
[10.1016/j.compgeo.2018.10.020](https://doi.org/10.1016/j.compgeo.2018.10.020)

Published: 01/02/2019

Document Version
Publisher's PDF, also known as Version of record

Published under the following license:
CC BY-NC-ND

Please cite the original version:
Tran, Q., & Sołowski, W. T. (2019). Generalized Interpolation Material Point Method modelling of large deformation problems including strain-rate effects – Application to penetration and progressive failure problems. *Computers and Geotechnics*, 106, 249-265. <https://doi.org/10.1016/j.compgeo.2018.10.020>

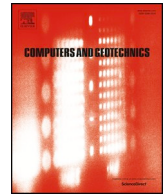
This material is protected by copyright and other intellectual property rights, and duplication or sale of all or part of any of the repository collections is not permitted, except that material may be duplicated by you for your research use or educational purposes in electronic or print form. You must obtain permission for any other use. Electronic or print copies may not be offered, whether for sale or otherwise to anyone who is not an authorised user.



ELSEVIER

Contents lists available at ScienceDirect

Computers and Geotechnics

journal homepage: www.elsevier.com/locate/compgeo

Research Paper

Generalized Interpolation Material Point Method modelling of large deformation problems including strain-rate effects – Application to penetration and progressive failure problems

Quoc-Anh Tran*, Wojciech Sołowski

Department of Civil Engineering, Aalto University, Espoo, Finland

ARTICLE INFO

Keywords:

Generalized Interpolation Material Point Method
 Large deformation modelling
 Strain rate effects
 Fall cone test
 Progressive failure
 Sensitive clays landslides

ABSTRACT

The article shows Generalized Interpolation Material Point Method numerical simulation of the Sainte Monique landslide. The simulation uses a strain-rate dependent Tresca constitutive model, extended with strain softening behaviour for structured clays. First, the paper replicates fall cone tests to validate the constitutive model and to select the material parameters. Afterwards, the paper shows the Sainte Monique landslide simulation which additionally considers shear band thickness to reduce the mesh-dependence. The results suggest that the strain-rate affects the prediction of the run-out distances and leads to the landslide acceleration-deceleration cycles (reported in, e.g. Corominas et al., 2005; Wang et al., 2010).

1. Introduction

Numerical methods allowing for very large deformation are of great interest in geotechnical engineering. For example, they may be used to predict the outreach and severity of the landslides and avalanches, as well as to simulate penetration problems. One family of the methods allowing for simulations of very large deformations are those stemming from the Material Point Method (MPM) by Sulsky et al. [3]. The Generalized Interpolation Material Point Method (GIMP) [4] is an evolution of the original MPM with an improved precision and stability and a method of choice for simulations shown in the paper.

Large deformation problems in geotechnics often involve penetration of a rigid body into the soil. MPM/GIMP was used to simulate a large number of those, including the penetration of a strip foundation [5], the pile installation into a sand layer [6] and the cone penetration test [7,8]. The mentioned studies ignored the strain rate effects during the penetration process. However, the strain rate effect of soft clays is one of the major factors influencing the undrained shear of soil in fall cone penetration test [9] as well as in the quickness test [10] and the penetration tests [11–13]. Therefore, the constitutive model used in all shown simulations incorporates the strain rate effects. The paper first validates the numerical technique (GIMP) and the constitutive model with the existing analytical solutions and experimental data for the fall cone penetration tests, extending the work of Tran et al. [14], while moving later to simulations of the 1994 Sainte Monique landslide.

Currently, there are many approaches to predict the progressive and retrogressive failure in sensitive clay landslides. For example, Puzrin et al. [15] and Quinn et al. [16,17] proposed methods based on the linear fracture mechanics and the evaluation of the length of existing shear band. Later, Zhang et al. [18,19] enhanced the method with a more realistic behaviour of the soil including elastic and non-linear strength degradation. These analytical models were applied to the inclined slopes with the failure driven by shear stresses induced by self-weight. However, the Sainte Monique landslide has a different characteristic. The landslide behaviour is highly nonlinear and time-dependent as the shear stress is affected by the progressive dislocation of softening soil mass. Additionally, the soil behaviour in the slide is rather complex. Therefore, it is necessary to use a numerical model to reproduce the progressive failure in Sainte Monique landslides instead of the methods [15–19].

Several numerical methods have been applied to study the spread failure of sensitive clays landslides including the Finite Element Method [20–22] and the coupled Eulerian - Lagrangian finite-element modelling [23,24]. Material Point Method has also been used to investigate the landslide failures [25–28] including progressive landslides [29] and levee failure [30]. However, in those studies, some key features of the sensitive clays influencing the progressive failure were rarely considered. Typically, the soil in the previous studies was taken as homogeneous, while the undrained shear strength of the natural normally consolidated clays typically increases linearly with depth. Several

* Corresponding author at: Department of Civil Engineering, Aalto University, Rakentajanaukio 4 A, 02150 Espoo, Finland.
 E-mail address: tran.quocanh@aalto.fi (Q.-A. Tran).

<https://doi.org/10.1016/j.compgeo.2018.10.020>

Received 5 April 2018; Received in revised form 16 October 2018; Accepted 31 October 2018

0266-352X/© 2018 The Authors. Published by Elsevier Ltd. This is an open access article under the CC BY-NC-ND license (<http://creativecommons.org/licenses/by-nc-nd/4.0/>).

studies suggested that ignoring the increase of the undrained shear strength with depth may overestimate the probability of failure of slope [31], strip footing [32] and tunnels [33]. Furthermore, studies [25–30] did not consider the strain rate effects affecting the shear strength of clays, which may play significant role in a landslide. For example, Wang et al. [2] reported that the increase of the residual shear strength with shear rate may be a reasonable explanation for the observed behaviour of the Shiraishi landslide. In the landslide, the rainfall induced a reduction of the undrained shear strength which caused a landslide acceleration, while the landslide acceleration resulted in the increase of undrained shear strength along the failure surface, which, in turn, caused a landslide deceleration. Similar cycles of shear strength changes and landslide movements were also described for the natural slope failure [34]. In addition, the strain rate also affects the characteristics of the post-failure. For example, neglecting the strain rate effects lead to an overestimation of the run-out distance of the sand columns [35,36] and the remoulded sensitive clays columns [10]. Therefore, this study considers the strain softening, increase of the undrained shear strength with depth and the strain rate effects to simulate sensitive clay landslide in Sainte-Monique, Quebec in 1994 including the progressive failure and the post-failure stage.

2. Generalized Interpolation Material Point method

The Material Point Method [3] is a numerical method, which can simulate the behaviour of materials described by continuum mechanics, similar to the Finite Element Method. In MPM, the material is discretised by the material points, which store the information required for the simulation. In the beginning of a time step, the data from the material points is transferred to the background grid, where the balance equations are solved. Afterwards, the material variables are updated and interpolated back to the material points. Usually, at the end of the time step, the initial configuration of the grid is reset.

In general, the Material Point Method is viewed as a meshfree/meshless method well-suited to solve the dynamic large displacement problems, for which the conventional Finite Element Method application is limited due to the mesh distortion. However, the original MPM has number of numerical instabilities, including the grid-crossing instability [37]. That instability is partially caused by the discontinuous gradient of the shape functions. The discontinuity in the shape function gradient results in a sudden change of the stress when a material point crosses to a new cell. These algorithmic errors are reduced in the newer formulations of MPM, such as Generalized Interpolation Material Point Method (GIMP) [4], the MPM using B-spline shape functions [38], the Dual Domain MPM (DDMP) [39] or the Convected Particles Domain Interpolation MPM (CPDI) [40]. This paper uses GIMP as encoded in the Uintah software (<http://uintah.utah.edu>). In this paper, the fall cone test simulation uses the shape functions of GIMP in axis-symmetry form [41] and the slope progressive failure simulation uses 3-dimensional formulation [4]. Details of the shape functions used in the simulations are presented in the Appendix.

3. Material behaviour of the clay

In the paper, the basic undrained behaviour of the clay is described by an elasto-plastic Tresca material model with a non-associated flow rule. All the simulations in the paper assume the dilation angle equal to 0 leading to no plastic volume change during shearing.

3.1. Effect of strain rate

The dependence of the undrained shear strength s_u on the shear strain rate $\delta\epsilon$ has been generally accepted for clays [42,43]. Considering the reference undrained shear strength $s_{u,ref}$ at a reference strain rate $\delta\epsilon_{ref}$, the effect of strain rate could be presented by a semi-logarithmic law [44,45] as:

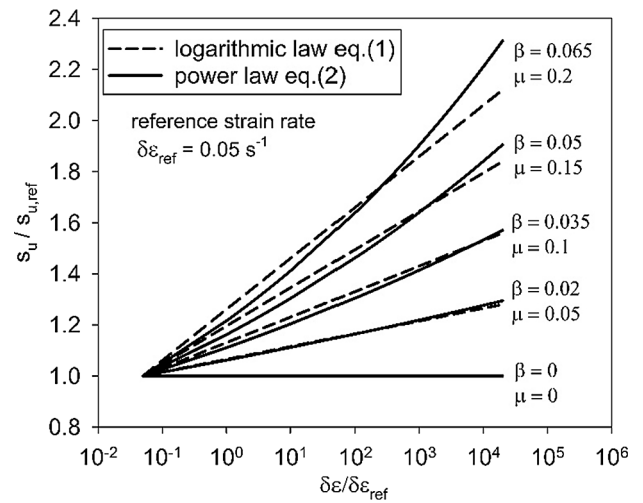


Fig. 1. Comparison between logarithmic law and power law.

$$\frac{s_u}{s_{u,ref}} = 1 + \mu * \log\left(\frac{\delta\epsilon}{\delta\epsilon_{ref}}\right) \tag{1}$$

However, this study assumes that the strain rate effects on the undrained shear strength s_u at a shear strain rate $\delta\gamma$ follow the more recently developed power law proposed by Einav and Randolph [46]:

$$\frac{s_u}{s_{u,ref}} = \left(\frac{\delta\gamma}{\delta\gamma_{ref}}\right)^\beta \tag{2}$$

The reason why the Eq. (2) is used instead of Eq. (1) is that in many clays the strain rate parameters μ are dependent on strain rates [47,11,48]. As such, μ may not necessarily be a suitable material constant. The power law (2) can capture the increase of the parameter μ with the change of the strain rate. Therefore, compared with semi-logarithmic law in Eq. (1) (linear in semi-logarithmic plot), a nonlinear fit in semi-logarithmic plot power law (2) may replicate the clay behaviour better (see Fig. 1). However, it may be worth noting that the other studies suggested that the strain rate parameter β is not perfectly constant either. Jeong et al. [49] argued that the strain rate parameter β used in the power law rheological model should be different for the intact and remoulded low-activity clays because of the difference in the fabrics and micro-structures. Nevertheless, this study assumes that the strain rate parameters (Eq.(2)) are constant in the clay materials simulated.

3.2. Effect of the plastic shear strength degradation

Apart from the strain rate effects, sensitive clays show a shear strength degradation with the increase of the plastic shear strains. After reaching the maximum shear strength, it is reducing due to the degradation of the sensitive clay structure. Therefore, the assumed constitutive model degrades the undrained shear strength with the increase of the shear strain [46] as follows.

$$s_u(\gamma, S_t) = s_{u,ref} \left[\frac{1}{S_t} + \left(1 - \frac{1}{S_t}\right) e^{-3\gamma/\gamma_{95}} \right] \tag{3}$$

where γ is the current accumulated shear strain, γ_{95} is the accumulated shear strains required to obtain 95% reduction of shear strength and the sensitivity S_t is the ratio of undisturbed over remoulded undrained shear strength $s_{ur,ref}$:

$$S_t = \frac{s_{u,ref}}{s_{ur,ref}} \tag{4}$$

3.3. Formulation of the undrained shear strength and elastic law

Based on the discussion above, the constitutive model used in the simulation assumes that the undrained shear strength could be described as a combination of the strain rate effects and the shear strength degradation terms taken as:

$$s_u(\delta\gamma, \gamma, S_t) = s_{u,ref} \left(\frac{\delta\gamma}{\delta\gamma_{ref}} \right)^\beta \left[\frac{1}{S_t} + \left(1 - \frac{1}{S_t} \right) e^{-\frac{3\gamma}{\gamma_{95}}} \right], \quad \gamma > \gamma_e \quad (5)$$

where the shear strain rate is computed from the strain rate tensor as:

$$\delta\gamma = \frac{1}{2} \sqrt{2(\delta\epsilon_{ii} - \delta\epsilon_{jj})^2 + 3\delta\epsilon_{ij}^2} \quad (6)$$

The reference undrained shear strength depends on the water content. The reference remoulded undrained shear strength in Eq. (5) can be described in power law as:

$$s_{u,ref}(w) = a_1 w^{-b_1} \quad (7)$$

where a_1 (kPa) is the undrained shear strength at $w = 100\%$ and at a reference strain rate $\delta\gamma_{ref}$ (kPa), w (%) is the water content and b_1 is the model parameter. The presented model has been validated by Boukpeti et al. [50,51].

Furthermore, while the strain rate influences greatly the undrained shear strength in the large deformation regime, in the small deformation regime the dynamic shear modulus also depends on the shear strain rate. Sorensen et al. [52] has shown that the dependence of the strain rate on the dynamic shear modulus, therefore, also the dynamic undrained shear modulus can be estimated as:

$$G_u(\delta\gamma) = G_{u,ref} \left(\frac{\delta\gamma}{\delta\gamma_{ref}} \right)^\beta, \quad \gamma \leq \gamma_e \quad (8)$$

The parameter β is the same as in Eq.(5), so the increase of the undrained shear modulus is proportional to the increase of the undrained shear strength. Therefore, the adopted formulation keeps the elastic shear strain value constant when the shear rate change. Fig. 2 depicts the degradation of the undrained shear strength with the increase of the accumulated shear strain for two different constant strain rates where $\delta\gamma_2 > \delta\gamma_1$, illustrating the implemented model (Eqs. (5) and (8)).

4. Modelling of fall cone tests

4.1. Problem definition

Fall cone test is a simple laboratory experiment used to determine the undrained shear strength and the sensitivity of the soft clays.

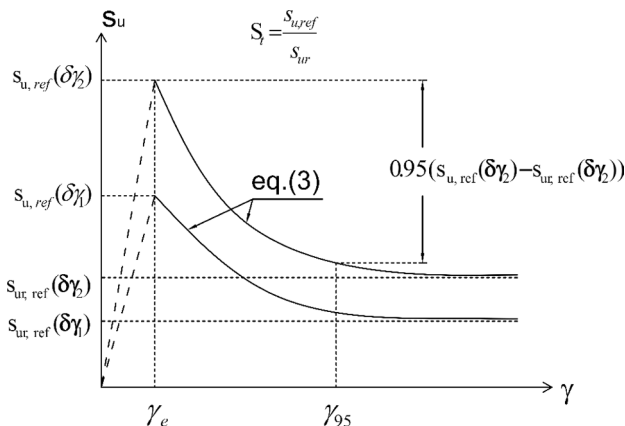


Fig. 2. Tresca model with strain rate and shear strength degradation.

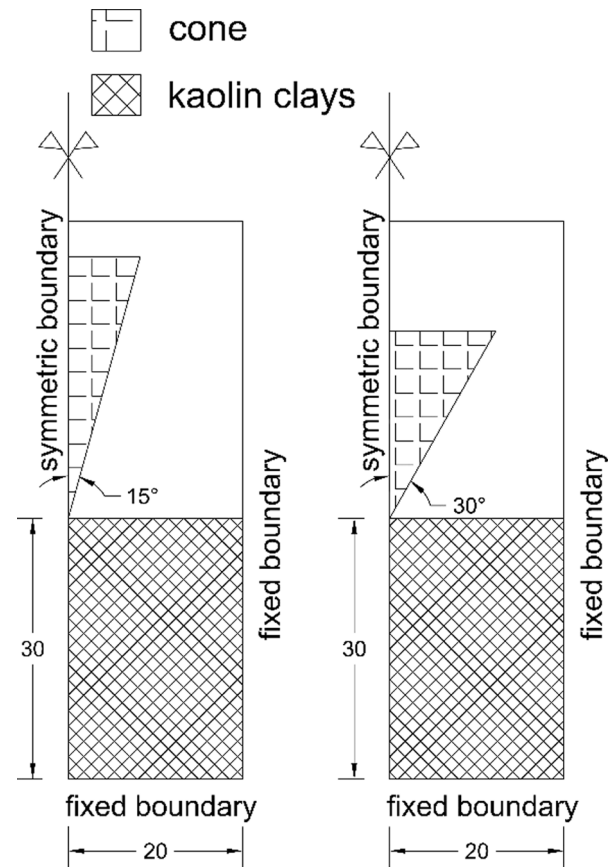


Fig. 3. Schematic of the 30° and 60° cone. Unit: mm.

Because the interpretation of the undrained shear strength depends on the strain rate effects [9], this paper validates the used computational framework by replication of fall cone tests with GIMP and the strain-rate dependent constitutive model. The framework is validated both against the theoretical solution of Koumoto and Houlsby [9] and the experimental data, with simulations of 30-degree and 60-degree standard cones (see Fig. 3).

The theoretical solution [9] used in the validation provides the undrained shear strength correlated to the cone penetration depth by means of a cone factor K . As the simulations assume rough contact between the soil and the cone, the cone factor for the rough cone was employed in the theoretical calculations.

The experimental data used in the validation comes from Hazell [53] who performed a series of fall cone experiments on the remoulded kaolin clays. Hazell [53] gives the cone vertical displacement and velocity based on the data obtained from a high-speed camera, post-processed with Particle Image Velocimetry analysis. The experiment also gives forces acting on the cone. Fig. 4 shows the experimental setup.

4.2. Constitutive parameters for kaolin clays

Hazell conducted the dynamic measurements of fall cone test experiments with artificial remoulded kaolin clays (mixing kaolin powder with water to reach different water contents). Therefore, the simulations used constitutive parameters (Table 1) based on the published data for these clays. Those were taken from Boukpeti et al. [50] who investigated remoulded kaolin clays during the solid fluid transition by measuring the remoulded undrained shear strength at different water contents. The parameters related to the influence of water content retrieved from those experimental data gave $a_1 = 0.205$ and $b_1 = 3.86$. Also, in the Hazell's experiment, the rough cone penetrated

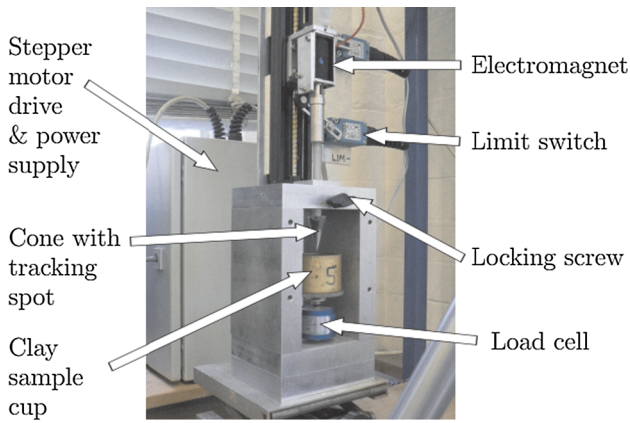


Fig. 4. Fall cone experiment setup [53]

Table 1
Parameters used in the fall cone simulations.

a_1 (kPa)	b_1	w (%)	$\delta\gamma_{ref}$ (s^{-1})	β	$G_{u,ref}$ (kPa)	ν_u	S_t
0.205	3.86	45–120%	0.5	0.06	$167s_{u,ref}$	0.49	1

approximately 20 mm which corresponds to kaolin clay with $s_{ur,ref} \approx 2.75$ kPa ($w = 51\%$), based on the theoretical solution of Koumoto and Housby [9].

The range of the strain rates in the free-falling cone tests are approximately from 1 to $10 s^{-1}$ and are roughly in the range of the strain rates in the vane shear tests (from 0.05 to $100 s^{-1}$) [54]. Therefore, the parameters for the strain rate effects for the fall cone test simulations could be calibrated based on the vane shear test from Boukpeti et al. [50], who performed the vane shear test for kaolin clays with different rotation rates. In [50], the minimum rotation rate 1%/s corresponds to the shear strain rate of about $0.5 s^{-1}$ [11]. This shear strain rate value was selected as the reference shear strain rate in the numerical model. Boukpeti et al. [50] have also shown that the strain rate parameter β , which is related to the increase of the undrained shear strength with the increase of the shear strain rate, was between 0.04 and 0.08 (see Fig. 5). That is similar to the increase of the resistance of penetrometers with the penetration rate given by Lehane et al. [12] with $\beta = 0.06–0.08$ and Chung et al. [55] with $\beta = 0.05–0.07$. Similarly, Rattley et al. [56] selected $\beta = 0.05$ based on triaxial tests for the centrifuge uplift tests. Based on the above suggestions, β is set to be 0.06 which seem to be a

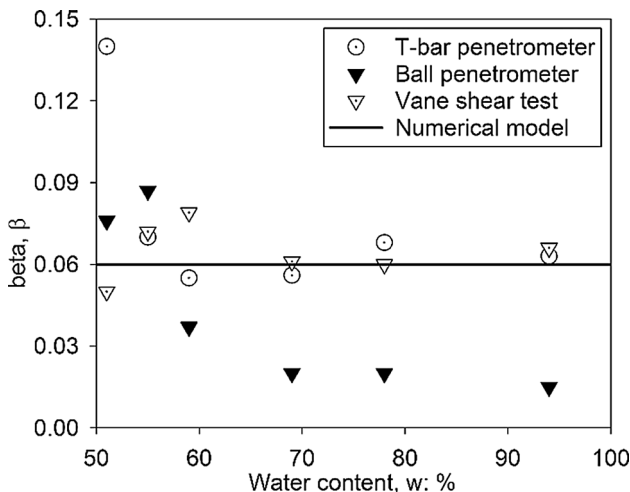


Fig. 5. Strain rate parameter β interpreted from experiment for kaolin clays [50]

reasonable average value for the numerical model. The reference undrained elastic modulus is set to be 167 times of the reference undrained shear strength, as suggested by Moavenian et al. [57]. Table 1 summarizes the parameters for the penetration simulations.

4.3. Validation of the model based on the fall cone tests on kaolin clays

In the fall cone test simulations, the theoretical undrained shear strengths of kaolin clays $s_{u,theo}$ are computed based on Eq. (7) with the given water contents w for the numerical model being:

$$s_{u,theo}(w) = 0.205w^{-3.86} \tag{9}$$

The calculated undrained shear strengths $s_{u,cal}$ in the fall cone simulations are computed based on the Koumoto and Housby [9] as:

$$s_{u,cal} = \frac{KQ}{d_p^2} \tag{10}$$

where Q (g) is the weight of the fall cone $Q = m \cdot g$ with m is the mass of the cone and g is the gravitational acceleration, d_p is the penetration depth obtained from the simulation and K is the cone factor. The cone factor depends on the type of the fall cone, cone roughness and the strain rate parameters. The simulation assumed that the contact between the cone and clay is rough. Therefore, the cone factors: $K = 1.03$ for 30° cone and $K = 0.25$ for 60° cone, are taken for the rough contact assumption [9].

In the shown simulations, the friction contact with the friction coefficient μ by Bardenhagen et al. [58] has been adopted. Fig. 6 shows the sensitivity analysis of the friction coefficient for the reference case with $s_{u,theo} = 2.75$ kPa and the 30° cone. The figure shows that higher friction coefficient than 0.2 does not change significantly the penetration depth – in other words, the friction coefficient of 0.2 is enough to prevent the sliding between cone and soil and can represent the rough cone, while minimising unwanted numerical effects related to e.g. interlocking effects [59,60] in nearly incompressible materials. As such, the friction coefficient of 0.2 was applied in all shown numerical analyses.

The number of background grid cells in GIMP plays a crucial role for the accuracy of the solution. Therefore, the grid density was varied to investigate how the number of cells affect the solution. The tested structured grid squares sizes ($h \times h$) were $h = 1, 0.5, 0.25, 0.16$ mm, each time with 9 material points per cell. These corresponds to 5400, 21,600, 86,400 and 211,500 material points in a simulation, respectively.

For the 100 g, 30° cone, the theoretical range of undrained shear strength is between 2 kPa and 10 kPa. Fig. 7 shows that the numerical

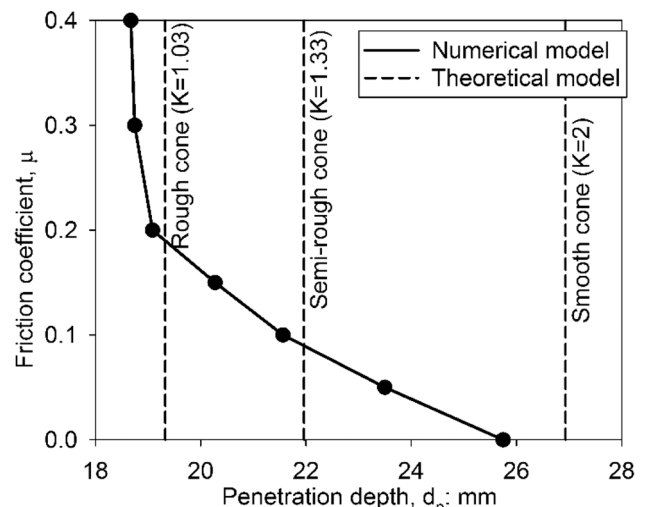


Fig. 6. Influence of friction coefficient in the penetration depth of 30° cone.

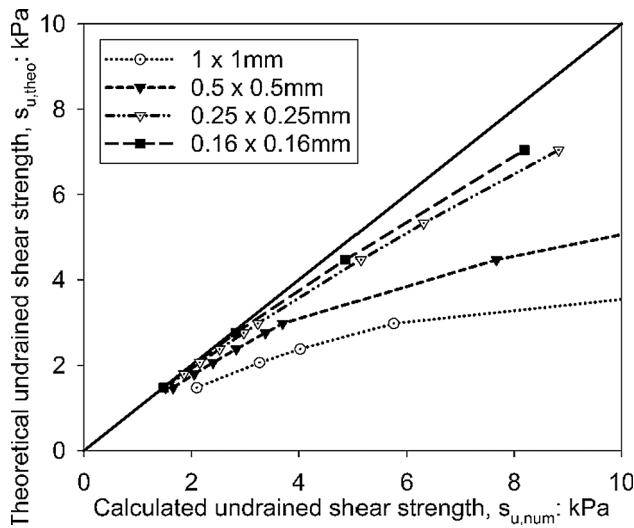


Fig. 7. Convergence of numerical undrained shear strength for 30° cone for square grid with size h between 1 mm and 0.16 mm.

simulations of the fall cone tests with a 30° cone converge well to the theoretical solutions at different assumed undrained shear strength. In the Fig. 7, the ideal solution would be such that the obtained undrained shear strength from the simulation, based on the simulated cone penetration and Eq. (10) would be the same as the assumed undrained shear strength of the soil in the simulation. In such case the points would be on the 45-degree line. Upon examination of Fig. 7 we observe that the correct solution is being approached with the increase in grid density.

To further examine the convergence rates of the numerical model, the error of the fall cone test is defined as a relative difference between the expected penetration depth $d_{p,theo}$ for the given theoretical undrained shear strength, based on Koumoto and Houlsby [9], and the penetration depth obtained in the numerical simulation $d_{p,cal}$ as:

$$\text{error} = \frac{d_{p,theo} - d_{p,cal}}{d_{p,theo}} \% \quad (11)$$

Fig. 8 shows that for 30° cone the errors clearly reduce as the number of grid cell increase. Notably, the errors for the higher penetration depth were smaller than for the shallower penetration depth. That can be perhaps explained by the unstructured grid used – for a higher undrained shear strength the expected penetration depth is

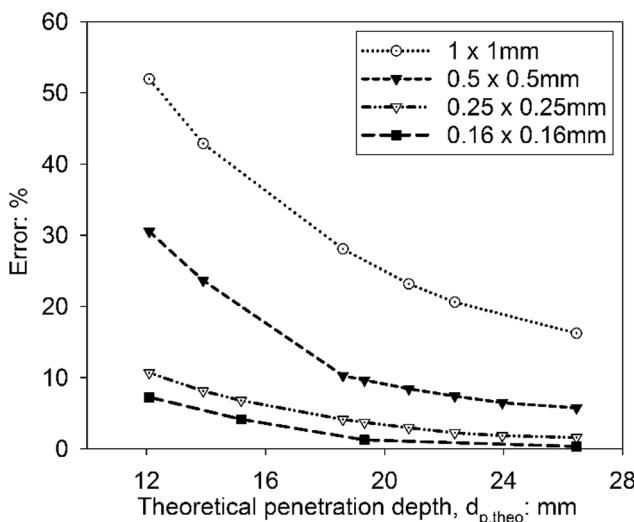


Fig. 8. Spatial errors of numerical solutions for 30° cone.

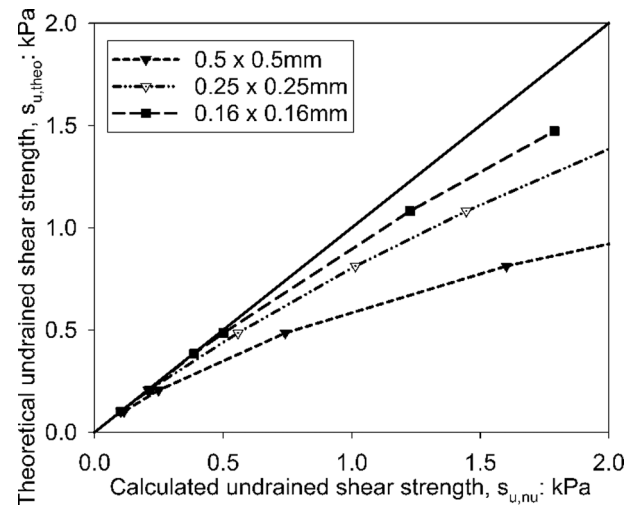


Fig. 9. Convergence of numerical undrained shear strength for 60° cone.

small, hence fewer material points are in the area of penetration. As such, a different grid, denser around the tip of the cone, would be more numerically efficient. Alternatively, for small penetration depths, the boundaries are far from the deformed material. Therefore, a smaller numerical domain with a denser mesh around the cone, without an increase in total number of material points, would be preferable. Nonetheless in the simulations, to allow for an easier comparison of results, always the same size of the problem was simulated.

Subsequently, the simulations were repeated for the 10 g 60° cone. Such a cone is commonly used in tests when the remoulded shear strength is expected to be lower than 2 kPa, which is typical for the very sensitive clays. Fig. 9 shows the convergence of the undrained shear strength obtained from simulations of 60° fall cone tests. The convergence rate trends are similar as in the 30° cone simulations. Again, the convergence to the correct results when shallower penetration is slower. For such low penetration depths, the grid in the simulation is also far from optimal.

Finally, in the simulations, the maximum normal stress on the cone is proportional to the undrained shear strength of the clay; therefore, the friction contact forces, which increase proportionally to the normal stresses, could increase significantly for the high strength materials. As such, the adopted contact law inaccuracies may have more impact on clays with higher undrained shear strength. Based on the sensitivity study (see Figs. 8 and 10), we expect the simulation results would

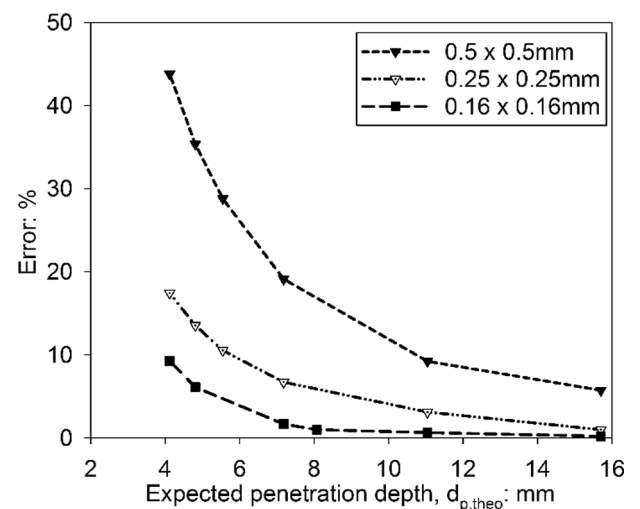


Fig. 10. Spatial errors of numerical solutions for 60° cone.

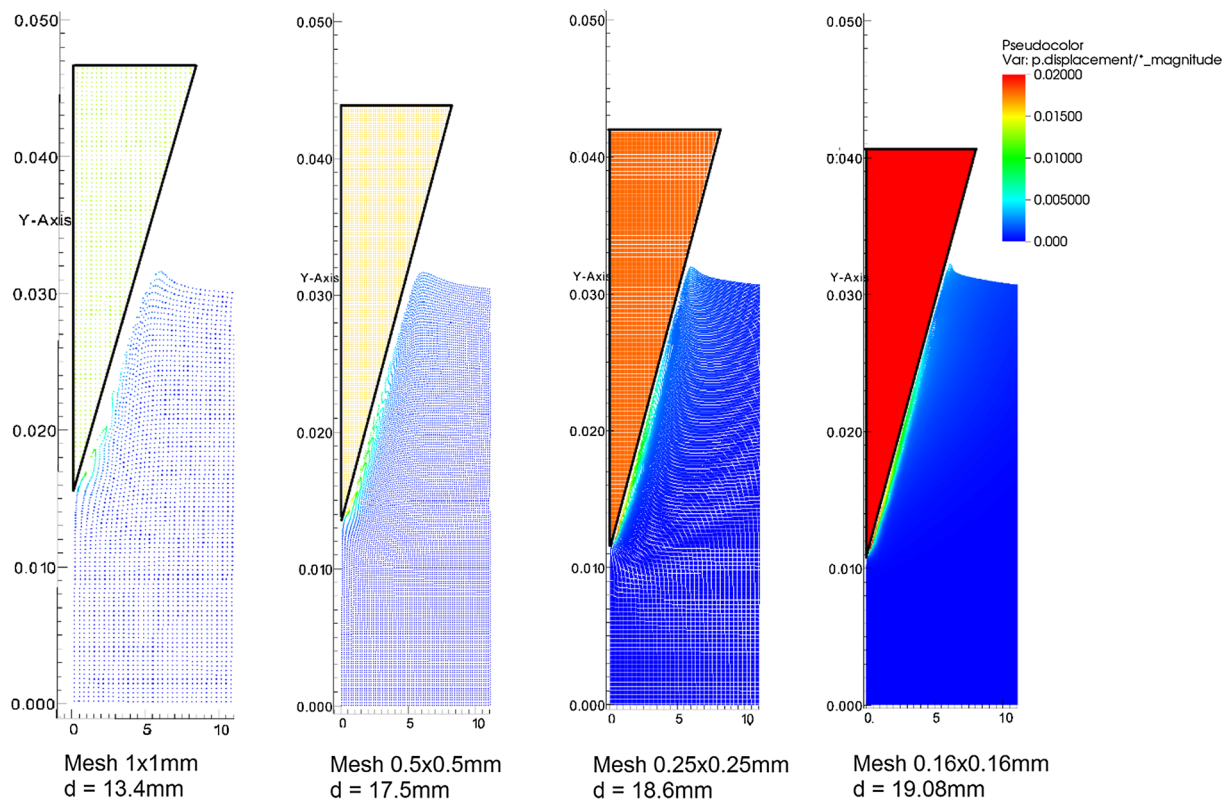


Fig. 11. Penetration depth of different mesh density.

converge to the analytical result, provided we use a much higher amount of material points and/or a differently denser structured grid (see Fig. 11). Therefore, we think it is unlikely that the contact law introduced systematic errors.

4.4. Simulation of the instrumented fall cone test on kaolin clay

Hazell [53] documented kinematics of the 100 g, 30° fall cone test. Simulation of such experiment provides further validation of the computational framework, as the simulated acceleration, velocity and force acting on the cone can be checked against the experimental values. In the experiment, the cone was free-falling into the kaolin clay body and reached the maximum penetration depth of 19.5 mm during approximately 0.1 s. Based on the penetration depth, the undrained shear strength calculated from Eq. (10) is 2.75 kPa with water content $w = 51\%$. The numerical simulation replicating the experiment used the parameters given in Table 1.

In general, the simulation replicates the experiment very well with grid size 0.16×0.16 mm and 9 material points per grid cell, the same grid size which gave accurate results in the previous validation. Fig. 12 shows the acceleration profile during the experiment and in the simulation. Notably, the acceleration at the very beginning of the experiment was lower than the gravitational acceleration because the cone was slowed down due to the friction mobilized in the cone shaft during the cone release for the free fall. To simulate those effects, the numerical model had a force acting in the opposite direction to the gravity which replicates the friction. The initial value of the force was 1 N and it was gradually reduced to 0 N after 0.01 s. From that time, the gravity was the only driver of the penetration process.

In the simulation, the cone acceleration oscillated close to the final value of the penetration. The amplitude of those oscillations reduced slowly. Those oscillations result from the assumed elastic behavior of the material and the explicit nature of the simulation leading to the elastic waves being reflected by the boundaries of the domain leading

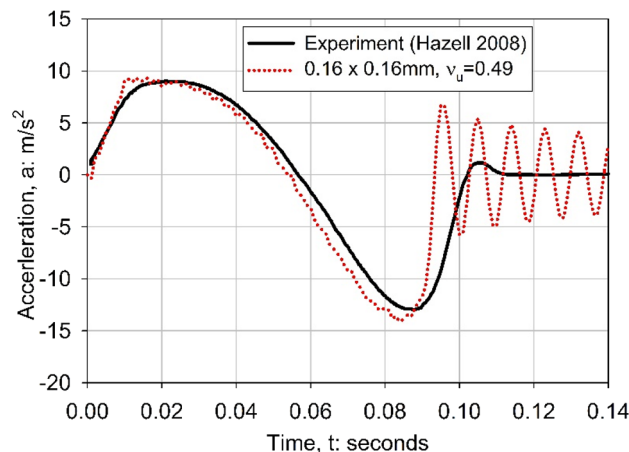


Fig. 12. Cone acceleration during penetration.

to oscillations. Those effects are only visible because there was no numerical damping applied in the simulation, to allow for the proper dynamic simulation of the whole process.

Figs. 13 and 14 show the convergence of the penetration depth and velocity compared with the experiment. The values of the displacement and the maximum velocity increase with the increase of grid density. However, the influence of Poisson’s ratio, examined for the finest grid, is not significant – there is very little difference between undrained Poisson’s ratio ν_u of 0.49 and 0.499. Therefore, Poisson’s ratio of 0.49 was selected for all simulations due to much lower computation time, as the time step depends on the bulk modulus value of the material.

Fig. 15 shows the forces acting on the cone in both the experiment and in the numerical simulations. The forces in the simulations at given penetration depth slightly decrease with the increase of grid density, leading to a very good agreement with the experiment at highest grid density. More importantly, the peak value of the force measurements

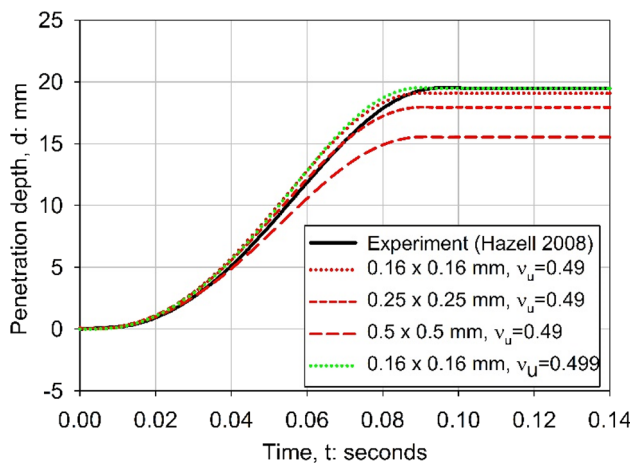


Fig. 13. Cone penetration depth vs. time.

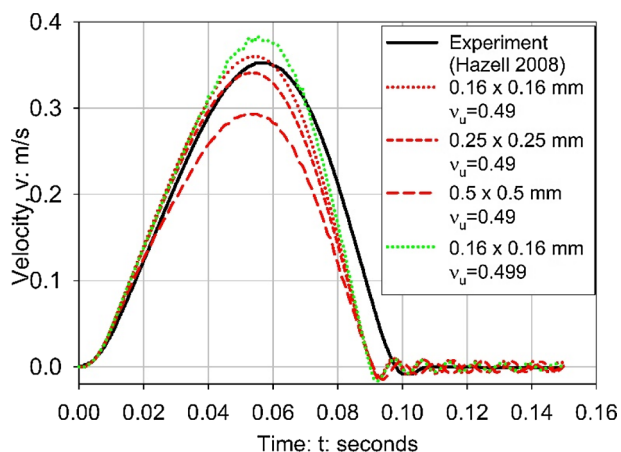


Fig. 14. Cone penetration velocity vs. time.

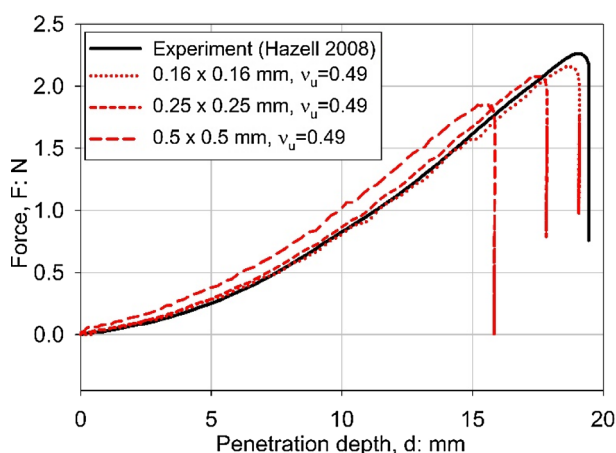


Fig. 15. Fall-cone forces during the penetration.

increased as the penetration depth increased and it practically converged to the experimental value at the grid density of 0.16×0.16 mm. As such, the simulations of the fall cone test agree with the experiment well.

In summary, the simulations of fall cone tests replicate very well the theoretical predictions and the experiment where strain rate is varying, giving some assurance that similar replication may be possible in larger scale simulations, such as those of progressive landslides. Similar validation, not included in this paper has been made based on the

spreading tests of sensitive clays [10], which again replicate the experiments well and give some assurance that the framework can be used to modelling of structured sensitive clays. As such, it seems that the developed modelling framework allows for rather accurate replication of undrained clay behaviour under dynamic conditions.

5. Modelling of progressive failure of the sensitive clays slope in Sainte-Monique, Quebec, Canada

According to the 2014-updated Varnes classification of landslides [61], the sensitive clay landslides can be divided into three categories: sensitive clay flowslides, translational progressive landslides and sensitive clay spreads. The concept of the progressive failure may help interpret the failure mechanism of the sensitive clay landslides. With that concept, the translational landslides could be considered as a downward progressive failure, because the trigger mechanism (e.g., embankment loading, piling) in the upslope area induces a failure surface propagating to the downslope area [62–66]. In contrast, the spreads could be classified as an upward progressive failure because the trigger mechanism (e.g., erosion, excavation) causes a horizontal failure surface propagating upwards [62,66–68]. Such upward progressive failure consists of two processes: (i) the propagation of a horizontal quasi-static failure surface (shear band) and (ii) the extension and dislocation of the soil mass above the remoulded shear surface, forming hosts and grabens. In 1994, a sensitive clay landslide occurred in Sainte-Monique, Quebec. The landslide was characterized as spreads failure with horsts and grabens observed in the site. In the subsequent sections, the paper will replicate numerically the upward progressive failure in the sensitive clay landslide in Sainte-Monique, Quebec, Canada in 1994.

5.1. Problem definition

This study investigates the progressive failure and post-failure of a sensitive clay landslide which occurred in Sainte-Monique, Quebec, Canada in 1994. Fig. 16 depicts the representative cross-section of the sensitive clay slope being basis for the 2D numerical model. The total initial height of the slope was about 16.7 m with the inclination of approximately 24° . The simulation used unit weight of the clay equal to 16 kN/m^3 . In the numerical model, the square grid resolution is 0.2×0.2 m with 4 material points per cell, leading to the total number of material points of approximately 500,000. The numerical analysis assumes that:

- even though the in-situ sensitive clay layer was very thick, simulation of only 5 m under the failure surface is sufficient. Sensitivity analyses made have shown that extra thickness added does not have significant influence on the results, while increases the number of material points significantly.
- the left and right boundary are fixed in the horizontal direction while the bottom boundary is fixed in the vertical direction.
- the initial stress condition was generated in drained condition with a typical drained shear strength of Canadian sensitive clays. Because the spread failure occurs rapidly, the soils was modelled in undrained condition with the initial undrained shear strength obtained from the soil investigations [68].
- the erosion at the toe of the slope triggered the failure of the slope. The progressive failure simulation represents the erosion as a small amount of soil excavated on the toe of the slope, see Fig. 16.
- the model does not consider several important features of natural sensitive clays such as anisotropy and creep. Long terms behaviour of the slope is not considered and as such the simulations neglect the long-term aspects of clay behaviour, related to effects such as fatigue, weathering and chemical effects. Those simplifications may be reassessed in the further research, which may consider more complexities of the clay behaviour.

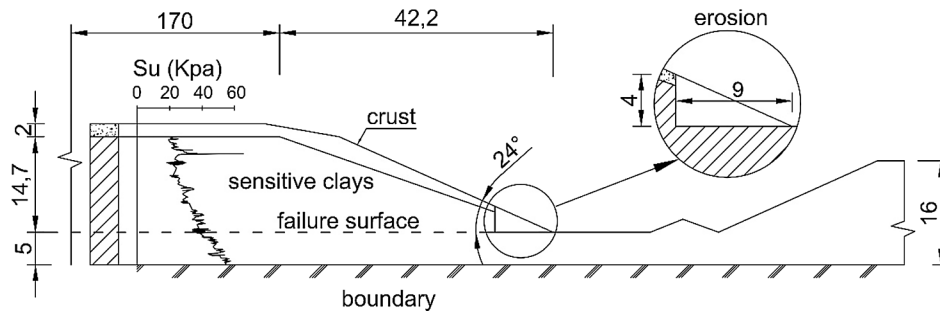


Fig. 16. Schematic of the slope used in the numerical model.

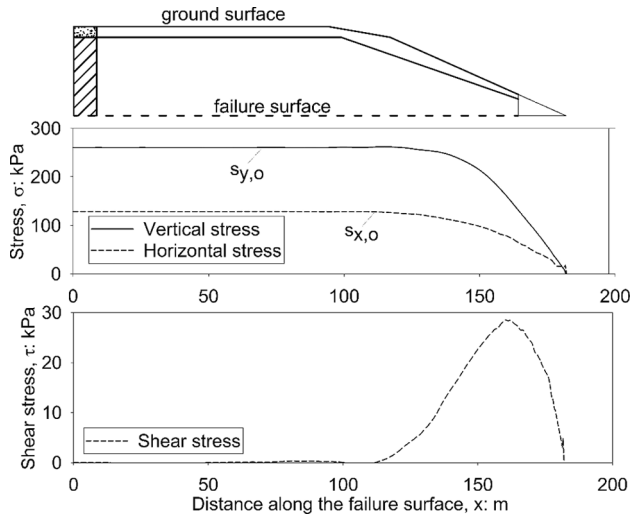


Fig. 17. Initial stress condition along the failure surface.

5.2. Pre-failure initial stress condition

Canadian sensitive clays, in drained condition, have typical value of cohesion (c') and friction angle (ϕ') of 10 kPa and 25–40°, respectively [69]. These values are obtained based on drained triaxial compression tests with the range of reconsolidation pressure of 5–30 kPa and pre-consolidation pressure from 100 to 400 kPa. In the numerical model, the sensitive clays are represented by the non-associated Mohr-Coulomb model with cohesion of 10 kPa, friction angle of 30° and zero dilatancy angle. The initial stress in the pre-failure condition was generated by the gravity loading. As the clay is normally consolidated, the earth pressure coefficient K_o was taken as 0.5. For the Mohr-Coulomb model, it corresponds to the Poisson's ratio is equal to 0.33 calculated from Eq. (12).

$$K_o = \frac{\sigma_h}{\sigma_v} = \frac{\nu}{1 - \nu} \tag{12}$$

Figs. 17 and 18 presents the initial stress in the failure surface observed on the site. The vertical and horizontal stress increase gradually from the toe of the slope upwards. Far away from the toe of the slope, the ratio of the horizontal and vertical stress at rest is equal to 0.5 (133.6 kPa/267.2 kPa). The shear stress increases to the maximum about 30 kPa at approximately 40 m from the toe of the slope and reduces to zero at 80 m from the toe of the slope.

5.3. Soil investigation and the numerical parameters of the sensitive clay

The soil investigation found a thick brown sand reaching 2 m from the ground surface. For the sake of simplicity, the undrained shear strength for this layer was taken as constant. Below the sand layer, there is a thick layer of a firm, sensitive, normally consolidated clay reaching the depth of 44 m. The undrained shear strength of that sensitive clays was determined by the fall cone tests, the vane shear test and the CPTUs. The undrained shear strength profile determined from these in-situ tests are used here to calibrate the numerical parameters of the constitutive model. The sensitive clays from 2 m to 10 m deep were slightly over-consolidated and interspersed with sandy layers. Below 10 m depth, the sensitive clays were normally consolidated with the undrained shear strength increasing linearly with depth. The intact undrained shear strength at a depth z can be approximated as:

$$s_{u,ref}(z) = \begin{cases} s_{u,z,ref}(z), & 2 \text{ m} \leq z < 10 \text{ m} \\ s_{u,z,ref}(z) + \Delta s_{u_i}(z - z_{ref}), & z \geq 10 \text{ m} \end{cases} \tag{13}$$

where $s_{u,z,ref}$ is the reference undrained shear strength at the reference depth $z_{ref} = 10$ m and Δs_{u_i} is the amount of the undrained shear strength increase per meter depth. With the sensitivity kept constant, the numerical model replicated the linear increase of the remoulded undrained shear strength observed on-site by the suitable reduction of the water content with depth, as given in Eq. (13). Fig. 19 shows the undrained shear strength in the numerical model and Fig. 20 compares

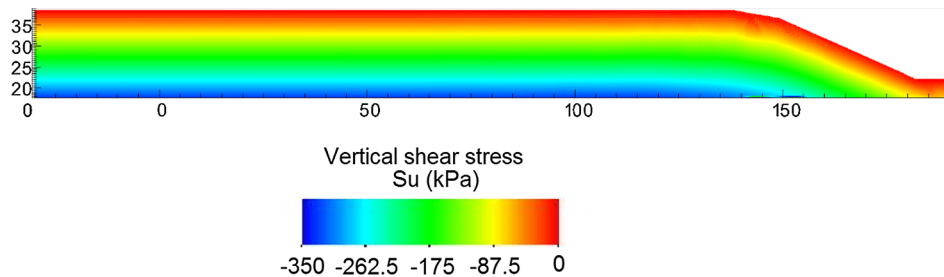


Fig. 18. Initial vertical stress of the slope.

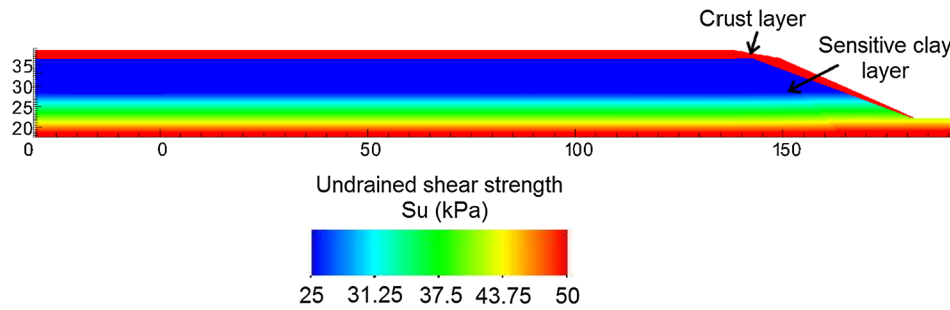


Fig. 19. Undrained shear strength of the slope.

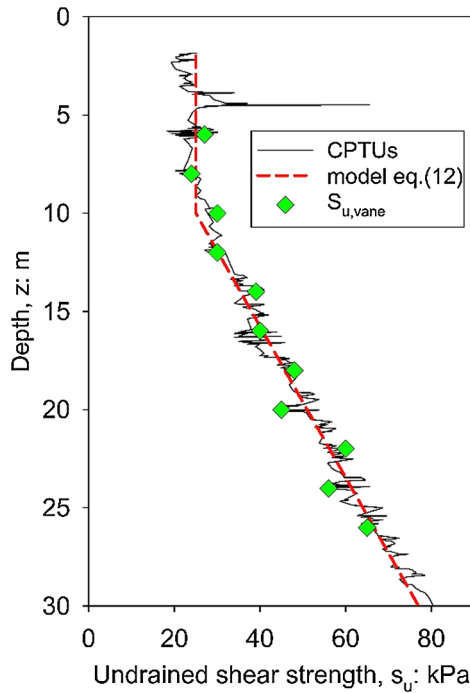


Fig. 20. Undrained shear strength profile [68]

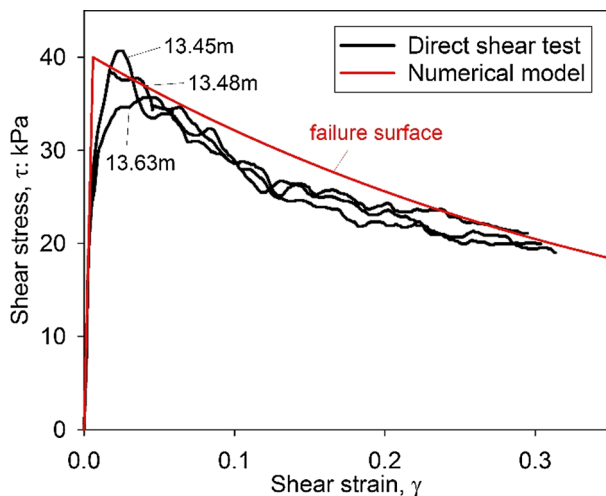


Fig. 21. Stress-strain behaviour in direct shear test [68]

the calibrated numerical model used and the data obtained based on the in-situ tests (CPTUs and vane shear tests). The $s_{u,z,ref} = 25$ kPa at $z_{ref} = 10$ m with the rate $\Delta s_u = 2.6$ kPa seem to be a reasonable

estimation.

In this study, the calculations used the undisturbed undrained shear strength obtained from the soil investigation (see Fig. 20) while the remoulded undrained shear strengths ranged from 0.7 kPa (value obtained from the fall cone test) to 10 kPa. Furthermore, the parameter γ_{95} was selected as 120% to replicate the softening behaviour observed in the direct simple shear tests (see Fig. 21). For the strain rate effects, the reference strain rate is 0.05 s^{-1} which corresponds to the shear strain rate of the standard van shear tests at the rotation rate of 0.1 deg/s [50]. For the undisturbed Canadian clays, the strain rate effects parameters μ in Eq. (1) are between 0.1 and 0.2 [43,45]. These values, with reference to Fig. 1, lead to the strain rate parameter β (in Eq. (2)) between 0.035 and 0.065. That is confirmed by other studies, e.g. [70], which suggested that for the intact sensitive clays β is in the range between 0.025 and 0.07. However, it should be noted that the value of strain rate parameters β could be higher for the remoulded sensitive clays [49] ($\beta = 0.05\text{--}0.17$ for the remoulded low-activity clays). As such, it is difficult to choose a single correct value of the strain rate parameter β for the clay. Therefore, several numerical analyses were performed with clay having the strain rate parameter β within the established range, that is between 0 and 0.17. Similar to the fall cone test, the dynamic shear modulus used was equal to $167 s_{u,ref}$, while the Poisson's ratio was taken as 0.49 due to undrained conditions. Table 2 summarizes the numerical parameters of sensitive clays.

The GIMP numerical results are sensitive to the grid density and number of material points. Therefore, to remove some of the mesh-dependency, a scaling law is applied to the numerical model by considering an embedded shear band [71], corresponding to the shear zone thickness of the shear band. The scaling law aims to keep the strain energy independent from the grid size. Considering the strain energy in the shear band (see Fig. 22), the increment of strain energy in the shear zone can be written as:

$$\dot{U}_{shear} = \frac{1}{2} V_{shear} \cdot \sigma \cdot \delta \epsilon_{shear} = \frac{1}{2} t_{shear} \cdot t_{FE} \cdot \sigma \cdot \delta \epsilon_{shear} \tag{14}$$

where V_{shear} is the volume of the representative square element in the shear band, t_{shear} is the thickness of the shear band, t_{FE} is the size of grid cell, σ is the stress and $\delta \epsilon$ is the strain in the shear band. In the numerical model, the strain energy is computed as:

$$\dot{U}_{model} = \frac{1}{2} V_{model} \cdot \sigma \cdot \delta \epsilon_{model} = \frac{1}{2} t_{FE} \cdot t_{FE} \cdot \sigma \cdot \delta \epsilon_{model} \tag{15}$$

where V_{model} is the volume of the representative square element in the numerical model. To obtain the same strain energy $\dot{U}_{model} = \dot{U}_{shear}$, the increment shear strain should be scaled as follow:

$$\delta \epsilon_{shear} = \frac{t_{FE}}{t_{shear}} \delta \epsilon_{model} \tag{16}$$

The shear zone thickness of the shear band is a critical parameter during the progressive failure. The shear zone of the sensitive clays can vary from 3 to 5 mm in the laboratory scale [72] to few decimetres in-situ [34,20]. In this study, we assume that the shear zone thickness t_{shear} is 0.2 m.

Table 2
Parameters in the progressive failure of the sensitive clays slope.

Layer	$s_{uz,ref}$ (kPa)	Δs_u (kPa)	z_{ref} (m)	S_t	γ_{95}	$\delta\gamma_{ref}$ (s ⁻¹)	β	$G_{u,ref}$ (kPa)	v_u	t_{shear} (m)	s_{ur} (kPa)
Crust	50	0	–	–	–	–	–	8350	0.49	–	–
Sensitive clay	25	2.6	10	4–55	1.2	0.05	0–0.17	$167s_{u,ref}$	0.49	0.2	$\frac{s_{u,ref}}{S_t}$

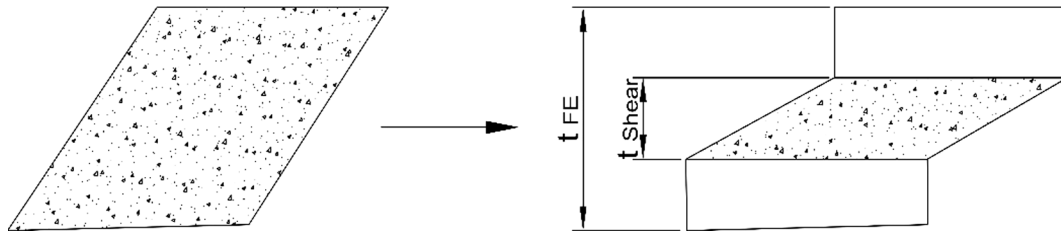


Fig. 22. Schematic of the scaling grid cell.

5.4. Result of progressive failure analysis

5.4.1. Influence of grid density

The grid density and the number of material points have influence on the numerical solutions in the Generalized Interpolation Material Point Method. For example, the prediction of run-out distance may be much affected by the grid density, as illustrated by Fig. 23, which shows different run-out distances for 2 different grids (0.2 × 0.2 m and 0.4 × 0.4 m) with the remoulded shear strength of 1.6 kPa and $\beta = 0.17$. As such, the simulations of the progressive failure include the shear band thickness (Eq. (14)–(16)) which reduces the grid-dependence of the numerical solution. To evaluate the efficiency of the al-

gorithm, the numerical model used 3 different cell sizes (0.4 m, 0.3 m, 0.2 m) with the remoulded shear strength of 1.6 kPa and $\beta = 0.17$. These grid cell sizes, with 4 material point per cell, correspond to approximately 180,000, 256,000 and 400,000 material points, respectively. Fig. 24 presents the contour map of all the progressive failure cases in the beginning of the stage at 5 s and 8 s. Visually, the orientation of the shear band as well as the kinematic behaviour (velocity, displacement) are similar between different grid densities. That means that taking into account the shear band thickness improves the simulation results and reduces greatly their dependence on grid density. To that end, Fig. 25 shows the final stage of the progressive failure for three grid densities. Again, in general, all the cases here gave a similar

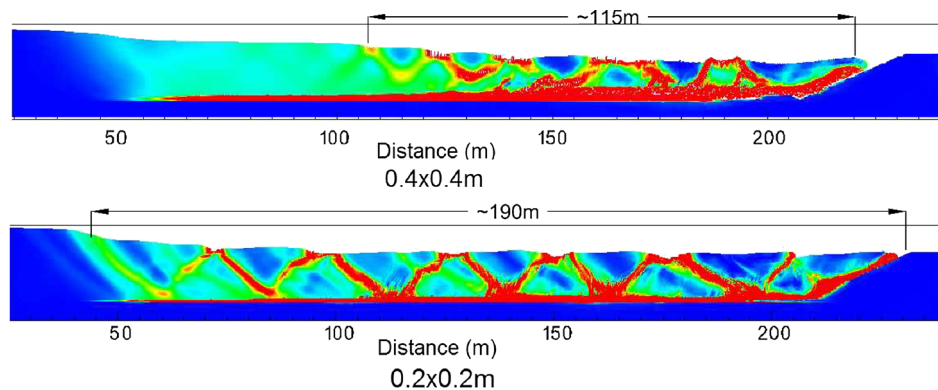


Fig. 23. Influence of grid size in the retrogression distance.

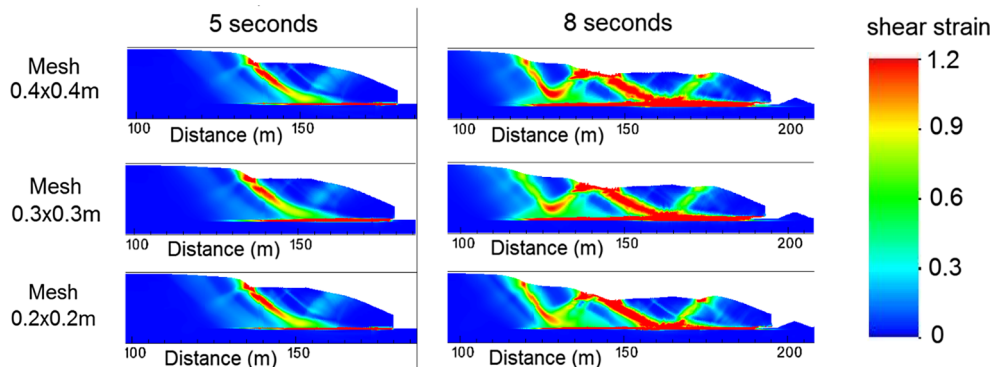


Fig. 24. Effect of mesh size on the numerical result at 5 s and 8 s.

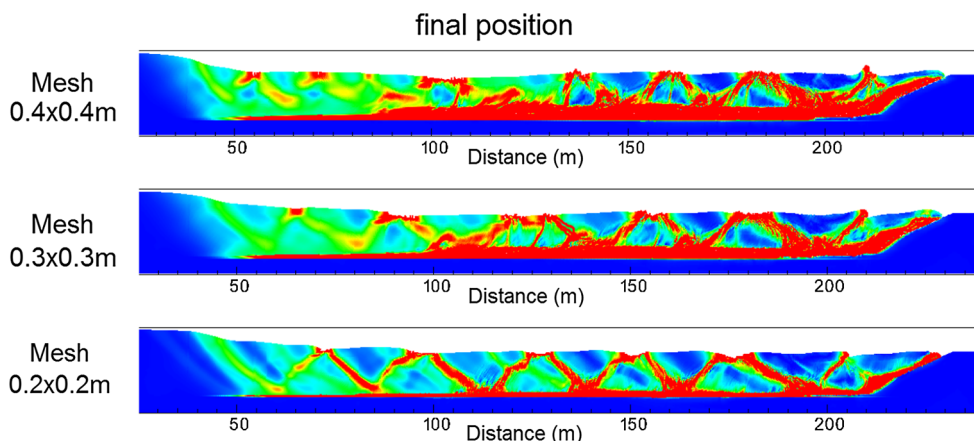


Fig. 25. Effect of mesh size on the numerical result at final stage.

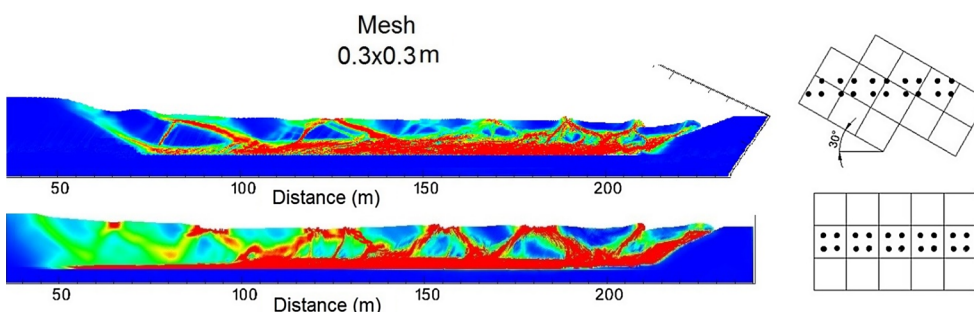


Fig. 26. Effect of grid orientation on the numerical result at final stage.

retrogressive distance of the sensitive clay landslide. However, still the more material points and denser grid leads to smaller errors, hence, the cell size 0.2 m was applied to analyse the Sainte-Monique landslide in greater detail.

5.4.2. Influence of grid orientation

The effects of grid orientation were investigated by considering 2 cases including a horizontal structured grid and a 30-degree inclined structured grid for grid size of 0.3×0.3 m (see Fig. 26). The grid rotation changes somewhat the orientation of the shear bands. In general, there is a similar failure pattern, including the horizontal failure surface and the multi-inclined shear bands above the failure surface. The influence of the grid orientation on the results needs further investigation. It perhaps might be mitigated with an anti-locking technique or mesh refinement. In this paper, we only apply the horizontal structured grid for the landslide simulations.

5.4.3. Influence of Poisson's ratio

Fig. 27 shows the influence of Poisson's ratio to the numerical

results for the finest grid 0.2×0.2 m. Two Poisson's ratios are selected for the comparison including 0.49 and 0.499. Visually, we observe that the landslide has a similar retrogression distances and similar shear band orientations for both calculations. Therefore, the Poisson's ratio of 0.49 was selected for all the landslide simulations as it leads to lower computational cost.

5.4.4. Sensitivity study on the propagation of failure

One of the important characteristics of the sensitive clay landslide is the retrogression distance. In the Sainte-Monique landslide, this retrogression distance was approximately 142 m in a representative cross section on-site. Fig. 28 shows the influence of the strain rate β on the retrogression distance of the sensitive clay landslide. In fact, the numerical model predicts the observed retrogression distance when the remoulded undrained shear strength at the failure surface are 1.6 kPa, 2.5 kPa and 3 kPa coupled with strain rate parameter β of 0, 0.06 and 0.17. These case correspond to the sensitivity of 25, 16 and 13.3 respectively.

The retrogression distance could be larger with the remoulded shear

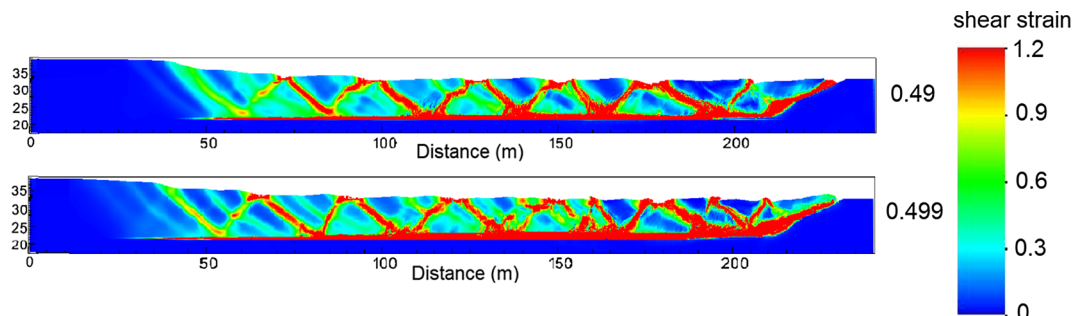


Fig. 27. Slope failure with Poisson's ratio of 0.49 and 0.499.

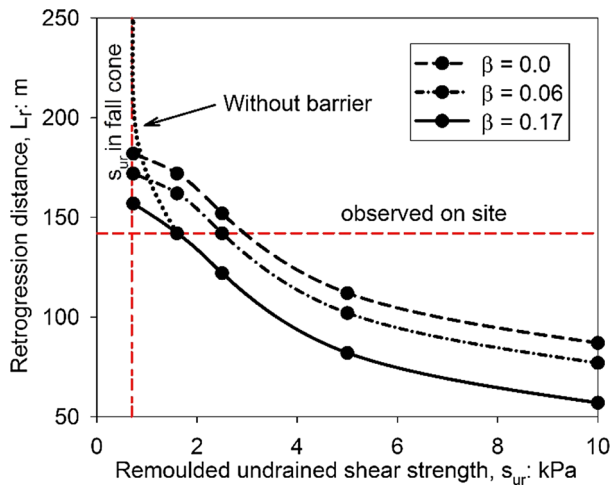


Fig. 28. Influence of strain rate in the retrogression distance.

strength at the failure surface $s_{ur} < 2$ kPa if there were no debris of the 1979 landslide (dark grey on the right in Fig. 30) acting as a barrier to block the debris flow of the 1994 landslide. Without the barrier, the retrogression distance could be very high such as for the case β of 0.17 (dot line marked without barrier in Fig. 28). In general, the inclusion of the strain rate effects in simulation led to the replication of the retrogression distance closer to the observed retrogression distance on site with the calculations using the remoulded undrained shear strength of 0.7 kPa determined from the fall cone test.

Because the Canadian sensitive clays typically have a high value of sensitivity ($S_t > 25$) and low value of remoulded undrained shear strength ($s_{ur} < 2$ kPa), the reference case with $s_{ur} = 1.6$ kPa, $S_t = 25$ and $\beta = 0.17$ was selected to analyze the global dynamic behaviour of the landslide. Fig. 29 presents the ground levels and failure surfaces observed on site and in the numerical model. The failure surface is almost planar and propagate from the toe of the slope to approximately 120 m.

5.4.5. Global dynamic analysis

In the Sainte-Monique landslides, the erosion near the river bank may have triggered the initial instability of the slope. In the numerical model, the erosion was represented by a small amount of soil excavated on the toe of the slope. Fig. 30 presents the numerical results from the initial condition to the post-failure state of the landslide in 5 s, 8 s, 16 s and 34 s with the shear strain contour map. The red colour denotes the clays in excessive shear strains ($\gamma > \gamma_{95} = 120\%$) and thus zones where the clays had been fully remoulded. To describe the failure process, we selected 4 points along the failure surface (B, C, E, G) for the analysis. The initial positions of these points are 123.73 m, 117.09 m, 82.56 m and 43.1 m.

In the beginning after 5 s, the erosion induced a thin horizontal shear band propagating from the toe of the slope upward to point B. The shear stress at point B reached the maximum value corresponding to the

current dynamic undrained shear strength of the sensitive clays (see Fig. 32) while the shear strain value along the current failure surface were very high. Therefore, the shear stress at that failure surface was already reduced and close to the remoulded undrained shear strength. Apart from the formation of the horizontal failure surface, the first failure of the slope occurred with a curve shear band propagating from the horizontal failure surface to the ground surface. After that, the horizontal failure surface was developing with the maximum shear stress point propagating from the toe of the slope to the points B, C, E and G at 5 s, 8 s, 16 s and 34 s respectively. During this process, above the horizontal failure surface, the neighbouring blocks were moving and dislocating. It was followed by a propagation of inclined shear bands between blocks from the horizontal failure surfaces (remoulded shear strength) to the ground surfaces. The sensitive clays inside the inclined shear bands became remoulded. The propagations of the inclined shear bands formed the horsts and grabens which are made from relatively undisturbed materials characterised by a high undrained shear strength.

To further investigate the dynamic motion of the landslide, Fig. 31 presents the numerical results with the velocity field contours of the soil mass at 4 different times since the initiation of the landslide (5 s, 8 s, 16 s and 34 s respectively). In general, each horsts and grabens had a similar lateral displacement rate (same colours of each blocks in Fig. 31), with the velocity increasing dramatically to approximately 4 m/s and reaching the equilibrium after 34 s.

In the presented numerical model, the complete upward progressive failure including the formation and propagation of the horizontal and inclined shear bands is replicated. However, it should be noted that the tip of the horst in the numerical model was around 90° while this angle was approximately 60° on-site. That discrepancy between observation and the numerical simulation may be due to the simplification of the constitutive model. It is likely that a more advanced constitutive model with effective stress analysis may be able to capture the correct shape of the horsts and grabens.

5.4.6. Stress-strain-strain rate relationship

As the upward progressive failure was successfully simulated, this section examines the influence of the strain rate on the shear stress and dynamic motion of the landslide. In the previous studies, Locat et al. [22] and Dey et al. [24] assumed that the peak undrained shear strength and peak shear stress along the failure surface were constant during the occurrence of the landslide because no strain rate effects were taken into account. To further investigate the shear stress along the horizontal shear band, Fig. 32 presents the mobilized shear stress and the corresponding shear strain rate for the maximum shear stress along the horizontal shear band. In general, along the failure surface, the peak shear stress values were approximately 40 kPa, a value close to the value obtained from the vane shear test in the field and the direct shear test (see Fig. 21). Notably, the peak shear stress values were not constant but correlated with the shear strain rate. The shear strain rate represents the rate of propagation speed of the horizontal failure surface. As the shear strain rate changes,

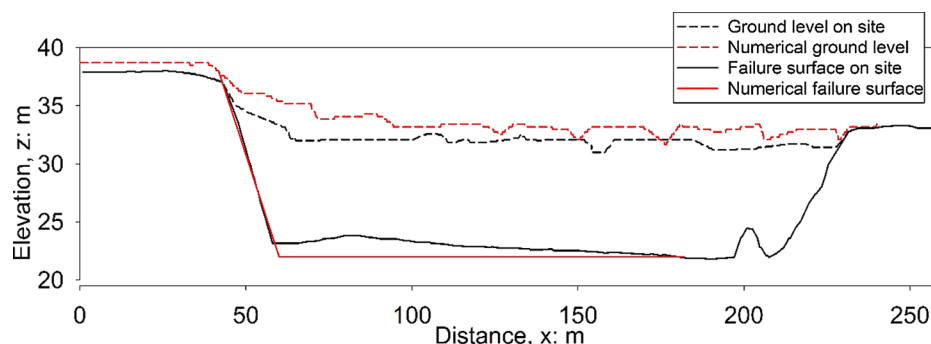


Fig. 29. Cross section for the representative case $s_{ur} = 1.6$ kPa, $\beta = 0.17$.

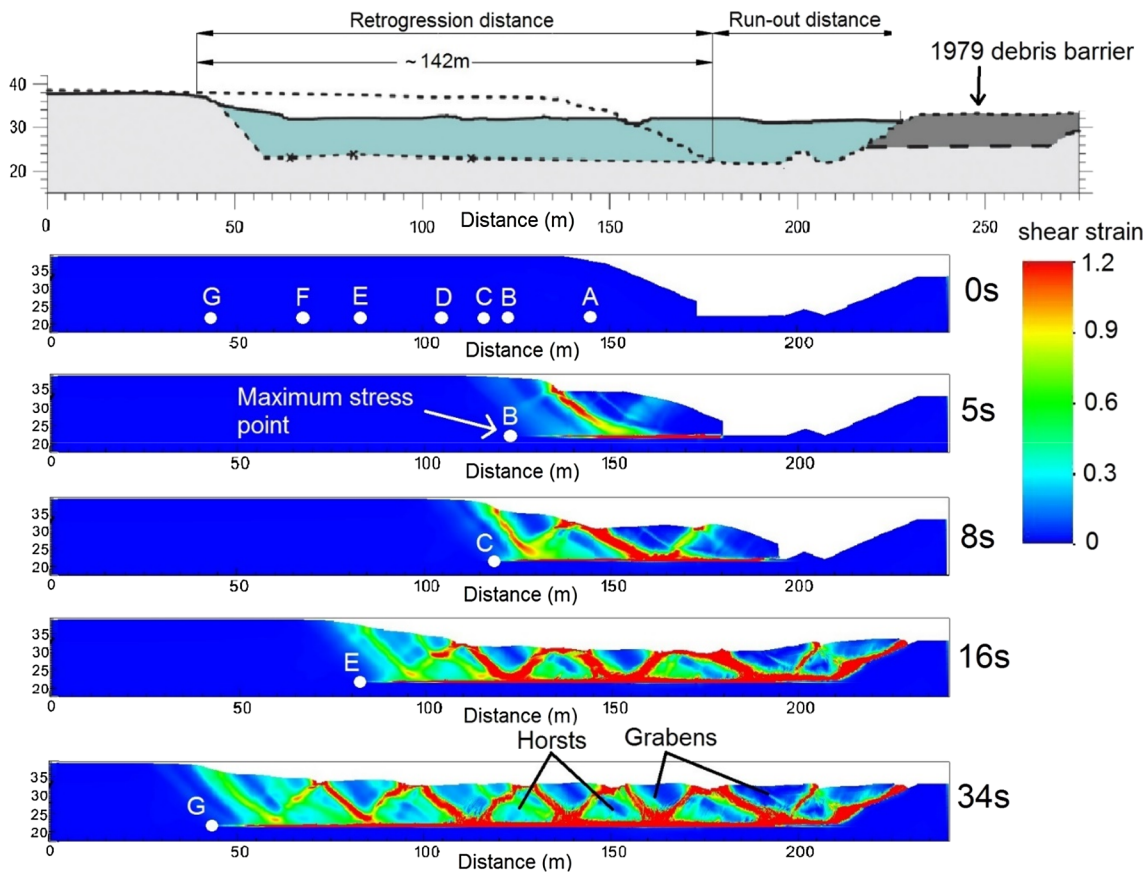


Fig. 30. Illustration of progressive failure of the sensitive clay slope.

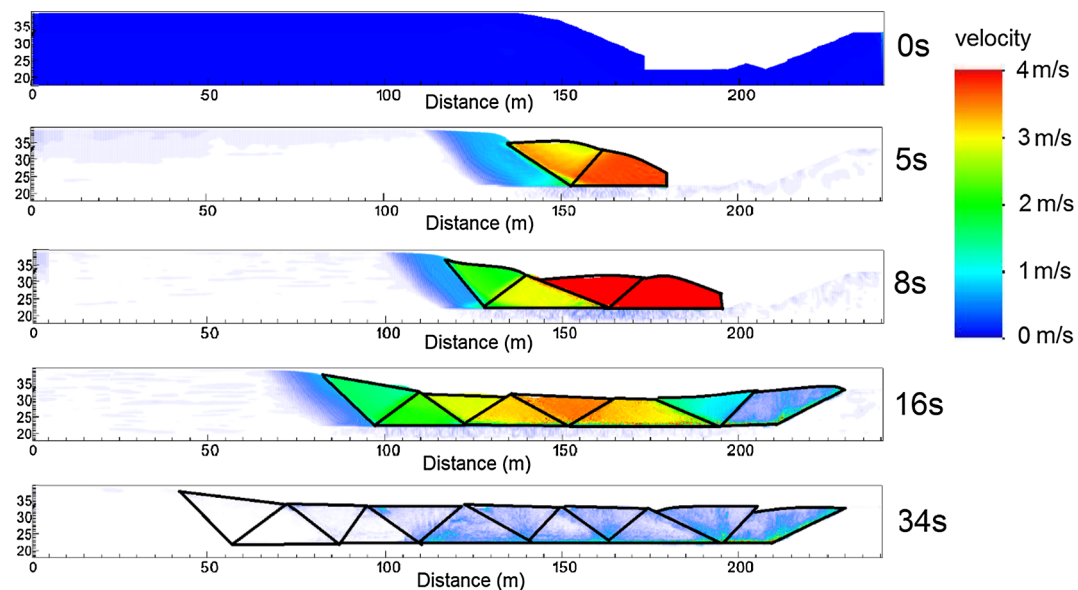


Fig. 31. Dynamic motion of the sensitive clay landslides.

the numerical analysis shows that the shear strain rate experienced a cycle of acceleration-deceleration.

Initially, the erosion induced an instability which caused the first acceleration. After 2 s, a high strain rate of 0.15 s^{-1} was observed at point A where the shear stress is, at that time, maximal. After that, the strain rate reduced significantly to 0.001 s^{-1} after 5 s at point B before increasing again to nearly 0.2 s^{-1} at point D after 10 s. Three cycles of acceleration-deceleration have been observed during the progressive

failure. After 34 s, the soil mass stopped moving and it reached the equilibrium condition.

To have a better understanding of the dynamic motion of the landslide at the post-failure, Fig. 33 shows the displacements of points A, D and F (see Fig. 30) along the horizontal shear failure. The material points near the toe of the slope have greater displacements and higher maximum velocities. Because the velocities of material points experienced the dynamic oscillations, Fig. 34 presents the smoothed velocity

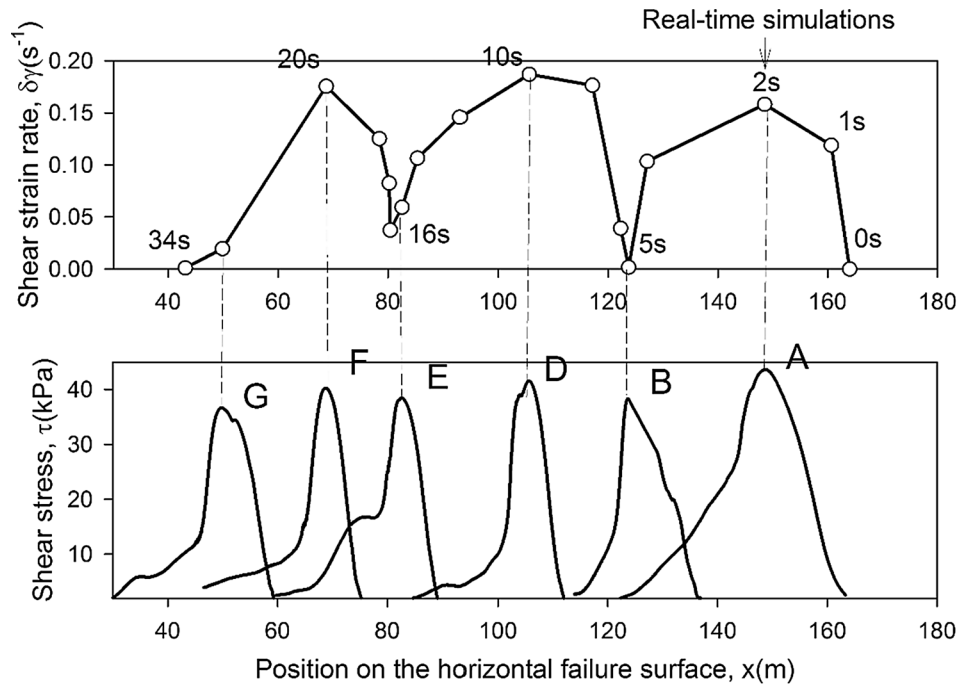


Fig. 32. Mobilized shear stress and shear strain rate on the horizontal failure surface.

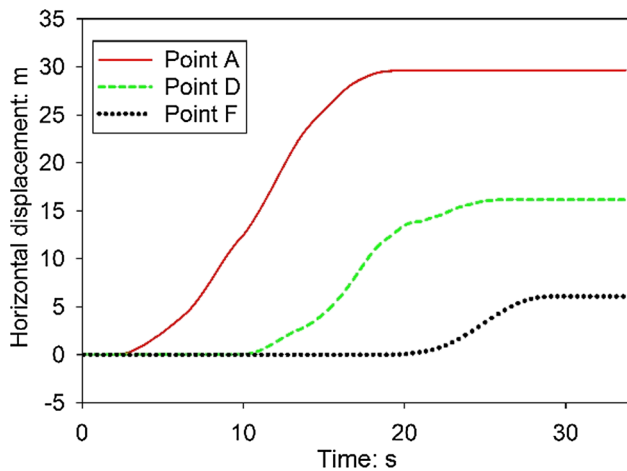


Fig. 33. Evolution of displacements in the landslides.

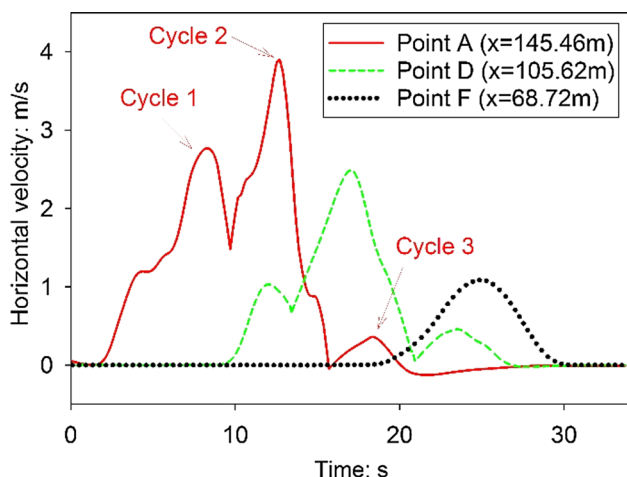


Fig. 34. Evolution of velocities in the landslides.

evolving with time. Point A and point D had 3 cycles of acceleration-deceleration movements because of the strain rate effects and the change of the geometry during the landslide. In contrast, point F had a lower maximum velocity, therefore, the strain effects were minimal and no extra acceleration-deceleration cycle occurred at this point.

In summary, the simulations suggest that the changes of undrained shear strength due to strain rate affect greatly the dynamic motion of the sensitive clays landslides. The simulations also show that changes of the shearing resistance due to the change of the strain rate could induce a cycle of the acceleration-deceleration movement. The acceleration-deceleration cycle occurs not only in the progressive failure phase, when the undrained shear strength changes with the strain rate, but also in the post-failure phase, when the velocity of the soil mass experiences a cycle of the acceleration-deceleration movement. That movement is similar to that shown in previous studies mentioning the acceleration-deceleration landslide motion for the catastrophic failures of landslides [73], Vallcebre landslide in Spain [1] and Shiraishi landslide in Japan [2]. In a slow-moving landslides such as creeping landslides, strain rate effects may be less pronounced, with perhaps other factors such as hydraulic conditions and thermal effects affecting the shear strength of the material and influencing the motion of the landslide. However, for a fast-moving landslide such as in Sainte-Monique, the strain rate effects seem to be significant and having a major influence on the landslide movement.

6. Conclusions

The paper validates the constitutive model and the Generalized Interpolation Material Point Method by replicating both theoretical and experimental solutions of the fall cone penetrometer tests. Subsequently, the paper shows a complete simulation of the upward progressive failure of the 1994 Sainte-Monique landslide. Based on the numerical analysis, we conclude that:

- In the fall cone simulations, the numerical solutions (penetration depth and calculated undrained shear strength) converge to the theoretical solutions with the increase of grid density. With the fine grid density as well as the strain-rate dependent constitutive model, GIMP can replicate the kinematic motion of the cone and forces acting to the soil during the penetration process.

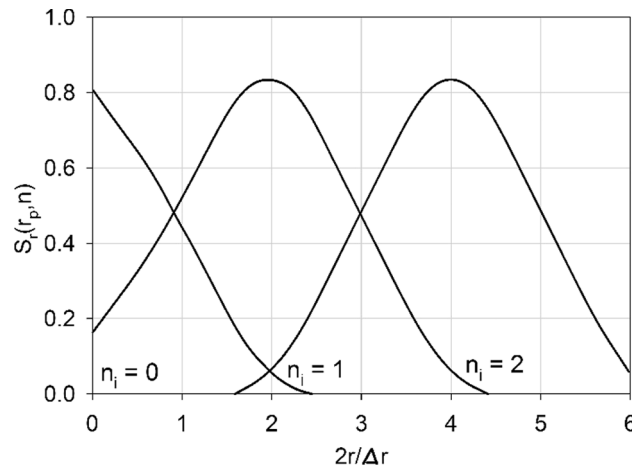


Fig. 35. Shape function in the radial direction r .

- In the progressive failure simulations, full process of sensitive clay landslide including propagation, formation of shear bands and dislocation of soil blocks is simulated, under assumption that the landslide was triggered by erosion near the toe of the slope. The simulation captures known feature of the landslide as well as the final spread well.
- Similar to the penetration simulations, the results of the progressive failure simulations depend on the grid density. However, employed scaling law which consider the shear band thickness reduced the mesh dependence of the numerical results.
- The numerical analysis showed that the large retrogression landslide can occur with the clays with high value of sensitivity ($S_t > 25$) and low value of remoulded undrained shear strength ($s_{ur} < 2$ kPa). Apart from the remoulded undrained shear strength and the degradation rate of the shear strength [22], the strain rate dependency of the undrained shear strength is a crucial factor for the prediction

of retrogression and run-out distances.

- The strain-rate effects lead to a significant change of the dynamic undrained shear strength during the progressive failure. The variation of the shear strength induces the change of the shear stress in the failure surface during the progressive failure and cycles of acceleration-deceleration movement in the post-failure.

Acknowledgements

This research was funded by the Academy of Finland, Finland under the project ‘Progressive failure and post-failure modelling of slopes with Generalized Interpolation Material Point Method (GIMP)’ under decision number 286628. The authors would like to thank Matti Lojander for providing references and data for the sensitive clays.

Appendix A. Shape function in axi-symmetry form in the applications of penetration tests [41]

For the axis-symmetry form with an element size $\Delta r \times \Delta z$ in the $r - z$ plane, the shape functions $S_{ip}(r, z, x_3)$ and the gradient of shape function of node $dS_{ip}(r, z, x_3)$ can be described as a function of a distance between the material point and the node in radial direction $r = r_p - r_i$ and vertical direction $z = z_p - z_i$, a current material point size $2l_p$ and a cell spacing $\Delta r, \Delta z$ [41]. The shape function of node ‘i’ is written as (see Fig. 35):

$$\xi_p = 2 \frac{r_p - r_i}{\Delta r}, \quad \eta_p = 2 \frac{z_p - z_i}{\Delta z} \quad \text{and} \quad n_i = \frac{r_i}{\Delta r} \tag{17}$$

$$S_r(\xi_p, n_i) = \begin{cases} \frac{(4-l_p)l_p - \xi_p^2}{4l_p} + \frac{\xi_p(\xi_p^2 - 3l_p^2)}{12l_p(2n_i + \xi_p)}, & |\xi_p| < l_p \\ \frac{2 - |\xi_p|}{2} - \frac{l_p^2}{6(2n_i + \xi_p)}, & l_p < |\xi_p| < 2 - l_p \\ \frac{(2+l_p - |\xi_p|)^2}{8l_p} \left(1 + \frac{2(1-l_p) - |\xi_p|}{3(2n_i + \xi_p)} \right), & 2 - l_p < |\xi_p| < 2 + l_p \\ 0, & \text{otherwise} \end{cases} \tag{18}$$

$$S_z(\eta_p) = \begin{cases} \frac{(4-l_p)l_p - \eta_p^2}{4l_p}, & |\eta_p| < l_p \\ \frac{2 - |\eta_p|}{2}, & l_p < |\eta_p| < 2 - l_p \\ \frac{(2+l_p - |\eta_p|)^2}{8l_p}, & 2 - l_p < |\eta_p| < 2 + l_p \\ 0, & \text{otherwise} \end{cases} \tag{19}$$

$$dS_r(\xi_p, n_i) = \begin{cases} -\frac{\xi_p}{2l_p} - \frac{l_p^2 - \xi_p^2}{4l_p(2n_i + \xi_p)}, & |\xi_p| < l_p \\ -\frac{1}{2} \text{sign}(\xi_p), & l_p < |\xi_p| < 2 - l_p \\ -\text{sign}(\xi_p) \frac{2+l_p - |\xi_p|}{4l_p} \left(1 + \text{sign}(\xi_p) \frac{2-l_p - |\xi_p|}{2(2n_i + \xi_p)} \right), & 2 - l_p < |\xi_p| < 2 + l_p \\ 0, & \text{otherwise} \end{cases} \tag{20}$$

$$dS_z(\eta_p) = \begin{cases} -\frac{\eta_p}{2l_p}, & |\eta_p| < l_p \\ -\frac{1}{2}\text{sign}(\eta_p), & l_p < |\eta_p| < 2 - l_p \\ -\text{sign}(\eta_p)\frac{2 + l_p - |\eta_p|}{4l_p}, & 2 - l_p < |\eta_p| < 2 + l_p \\ 0, & \text{otherwise} \end{cases} \quad (21)$$

$$S_{ip}(r, z, \theta) = S_r(\xi_p, n_i)S_z(\eta_p)S_{ip}(\theta) \quad (22)$$

$$\mathbf{G}_{ip}(r, z, \theta) = \left(\frac{2}{\Delta r} dS_r(\xi_p, n_i)S_z(\eta_p), \frac{2}{\Delta z} S_r(\xi_p, n_i)dS_z(\eta_p), S_{ip}(\theta) \right) \quad (23)$$

$$\mathbf{T}_{ip}(r, z, \theta) = \frac{2}{\Delta r(2n_i + \xi_p)} S_z(\xi_p)S_z(\eta_p)S_{ip}(\theta) \quad (24)$$

The gradient of the shape function $\mathbf{G}_{ip}(r, z, \theta)$ and $\mathbf{T}_{ip}(r, z, \theta)$ are used to update the nodal internal forces as follows:

$$f_i^{int} = - \sum_p m_p \sigma_p(r, z) \mathbf{G}_{ip}(r, z, \theta) - \sum_p m_p \sigma_p(\theta) \mathbf{T}_{ip}(r, z, \theta) \quad (25)$$

Appendix B. Shape function in plane strain form in the applications of progressive failure [4]

For the plane strain form with an element size $h \times h$, the shape functions $S_{ip}(x_1, x_2, x_3)$ and the gradient of shape function $dS_{ip}(x_1, x_2, x_3)$ can be described as a function of a distance between the material point (x_p) and the node(x_i) $x = x_p - x_i$, a current material point size $2l_p$ and a cell spacing h [4]:

$$S_{ip}(x) = \begin{cases} 1 - \frac{x^2 + l_p^2}{2hl_p}, & |x| < l_p \\ 1 - \frac{|x|}{h}, & l_p < |x| < h - l_p \\ \frac{(h + l_p - |x|)^2}{4hl_p}, & h - l_p < |x| < h + l_p \\ 0, & \text{otherwise} \end{cases} \quad (26)$$

$$dS_{ip}(x) = \begin{cases} -\frac{x}{hl_p}, & |x| < l_p \\ -\left(\frac{1}{h}\right)\text{sign}(x), & l_p < |x| < h - l_p \\ \frac{-\text{sign}(x)(h + l_p - |x|)}{2hl_p}, & h - l_p < |x| < h + l_p \\ 0, & \text{otherwise} \end{cases} \quad (27)$$

$$S_{ip}(x_1, x_2, x_3) = S_{ip}(x_1)S_{ip}(x_2)S_{ip}(x_3) \quad (28)$$

$$dS_{ip}(x_1, x_2, x_3) = (dS_{ip}(x_1)S_{ip}(x_2)S_{ip}(x_3), dS_{ip}(x_2)S_{ip}(x_1)S_{ip}(x_3), dS_{ip}(x_3)S_{ip}(x_1)S_{ip}(x_2)) \quad (29)$$

The gradient of the shape function $dS_{ip}(x_1, x_2, x_3)$ is used to update the nodal internal forces:

$$f_i^{int} = - \sum_p m_p \sigma_p(x_1, x_2, x_3) dS_{ip}(x_1, x_2, x_3) \quad (30)$$

Appendix C. Supplementary data

Supplementary data to this article can be found online at <https://doi.org/10.1016/j.compgeo.2018.10.020>.

References

- [1] Corominas J, Moya J, Ledesma A, Lloret A, Gili JA. Prediction of ground displacements and velocities. *Landslides* 2005;2:83–96.
- [2] Wang G, Suemine A, Schulz W. Shear rate dependent strength control on the dynamics of rainfall-triggered landslides, Tokushima Prefecture, Japan. *Earth Surf Proc Land* 2010;35(4):407–16.
- [3] Sulsky D, Chen Z, Schreyer HL. A particle method for history-dependent materials. *Comput Methods Appl Mech Eng* 1994;118(1–2):179–96.
- [4] Badenhagen SG, Kober EM. The generalized interpolation material point method. *Comput Model Eng Sci* 2004;5:477–95.
- [5] Sotowski W, Sloan S. Evaluation of material point method for use in geotechnics. *Int J Numer Anal Meth Geomech* 2015;39:685–701.
- [6] Phuong N, van Tol A, Elkadi A, Rohe A. Numerical investigation of pile installation effects in sand using material point method. *Comput Geotech* 2016;73:58–71.
- [7] Ceccato F, Beuth L, Vermeer P, Simonini P. Two-phase Material Point Method applied to the study of cone penetration. *Comput Geotech* 2016.
- [8] Ceccato F, Beuth L, Simonini P. Analysis of piezocone penetration under different drainage conditions with the two-phase material point method. *J Geotech Geoenviron Eng* 2016;142(12).
- [9] Koumoto T, Houslyby GT. Theory and practice of the fall cone test. *Geotechnique* 2001;51(8):701–12.
- [10] Tran QA, Sotowski W, Karstunen M. Modelling of the quickness test of sensitive clays using the generalized interpolation material point method. In: 2nd international workshop on landslides in sensitive clays, Trondheim, Norway; 2017.
- [11] Einav I, Randolph M. Effect of strain rate on mobilized strength and thickness of curved shear bands. *Geotechnique* 2006;56(7):501–4.
- [12] Lehane B, Loughlin C, Gaudin C, Randolph M. Rate effects on penetrometer resistance in kaolin. *Geotechnique* 2009;59(1):41–52.
- [13] DeJong J, Yafate N, DeGroot D. Evaluation of Undrained Shear Strength using Full Flow penetrometers. *J Geotech Geoenviron Eng* 2011;137(1):14–26.
- [14] Tran QA, Sotowski W, Karstunen M, Korkiala-Tanttu L. Modelling of fall-cone tests with strain-rate effects. *Procedia Eng* 2017;175:293–301.
- [15] Puzrin AM, Germanovich LN. The growth of shear bands in the catastrophic failure of soils. *Proc Roy Soc A* 2005;461(2056):1199–228.
- [16] Quinn P, Diederichs M, Rowe R, Hutchinson D. Development of progressive failure in sensitive clay slopes. *Can Geotech J* 2012;49(7):782–95.

- [17] Quinn P, Diederichs M, Rowe R, Hutchinson D. A new model for large landslides in sensitive clay using a fracture mechanics approach. *Can Geotech J* 2011;48(8):1151–62.
- [18] Zhang W, Wang D, Randolph MF, Puzrin AM. Catastrophic failure in planar landslides with a fully softened weak zone. *Geotechnique* 2015;65(9):755–69.
- [19] Zhang W, Wang D, Randolph MF, Puzrin AM. Dynamic propagation criteria for catastrophic failure in planar landslides. *Int J Numer Anal Meth Geomech* 2016;40:2312–38.
- [20] Andresen L, Jostad HP. Numerical modeling of failure mechanisms in sensitive soft clays - application to offshore hazards. In: *Proceedings of the offshore technology conference, Houston, TX; 2007*.
- [21] Andresen L, Jostad H. Analyses of progressive failure in long natural slope. In: *Proceedings of the 9th symposium on numerical models in geomechanics - NUMOG IX, Ottawa, Ontario; 2004*.
- [22] Locat A, Jostad H, Leroueil S. Numerical modeling of progressive failure and its implications for spreads in sensitive clays. *Can Geotech J* 2013;50:961–78.
- [23] Dey R, Hawlader B, Phillips R, Soga K. Modeling of large-deformation behaviour of marine sensitive clays and its application to submarine slope stability analysis. *Can Geotech J* 2016;53:1138–55.
- [24] Dey R, Hawlader B, Phillips R, Soga K. Large deformation finite element modelling of progressive failure leading to spread in sensitive clay slope. *Geotechnique* 2015;65(8):657–68.
- [25] Andersen S, Andersen L. Modelling of landslides with material point method. *Comput Geosci* 2010;14(1):137–47.
- [26] Llano-Serna M, Farias MM, Pedrosa DM. An assessment of the material point method for modelling large scale run-out processes in landslides. *Landslides* 2016;13(5):1057–66.
- [27] Li X, Wu Y, He S, Su L. Application of the material point method to simulate the post-failure. *Eng Geol* 2016;212:1–9.
- [28] Yerro A, Alonso EE, Pinyol NM. Run-out of landslides in brittle soils. *Comput Geotech* 2016;80:427–39.
- [29] Wang B, Vardon P, Hicks MA. Investigation of retrogressive and progressive slope failure mechanisms using the material point method. *Comput Geotech* 2016;78:88–98.
- [30] Bandara S, Soga K. Coupling of soil deformation and pore fluid flow using material point method. *Comput Geotech* 2015;63:199–214.
- [31] Li DQ, Qi XH, Phoon KK, Zhang LM, Zhou CB. Effect of spatially variable shear strength parameters with linearly. *Struct Saf* 2014;49:45–55.
- [32] Li DQ, Qi XH, Cao XJ, Tan WZ, Phoon KK, Zhou CB. Reliability analysis of strip footing considering spatially variable undrained shear strength that linearly increases with depth. *Soils Found* 2015;55(4):866–80.
- [33] Wilson D, Abbo A, Sloan S, Yamamoto K. Undrained stability of rectangular tunnels where shear strength increases linearly with depth. *Can Geotech J* 2017;54(4):469–80.
- [34] Leroueil S. Natural slopes and cuts: movement and failure mechanisms. *Geotechnique* 2001;51(3):197–243.
- [35] Liang DF, He XZ. A comparison of conventional and shear-rate dependent Mohr-Coulomb models for simulating landslides. *J Mountain Sci* 2014;11(6):1478–90.
- [36] He X, Liang D. Study on the runout of granular columns with SPH. *Int J Offshore Polar Eng* 2015;25(4):281–7.
- [37] Zhou S. The Numerical Prediction of Material Failure Based on the Material Point Method PhD thesis Department of Mechanical Engineering, University of New Mexico; 1998.
- [38] Steffen M, Kirby R, Berzins M. Analysis and reduction of quadrature errors in the Material Point Method (MPM). *Int J Numer Meth Eng* 2008;76:922–48.
- [39] Zhang B, Ma X, Giguere P. Material Point Method enhanced by modified gradient of shape function. *J Comput Phys* 2011;230:6379–98.
- [40] Sadeghirad A, Brannon Rebecca M, Burghardt J. A convected particle domain interpolation technique to extend applicability of the material point method for problems involving massive deformations. *Int J Numer Meth Eng* 2011;86:1435–56.
- [41] Nairn J, Guilkey J. Axisymmetric form of the generalized interpolation material point method. *Int J Numer Method Eng* 2015;101:127–47.
- [42] Leroueil S, Kabbaj M, Tavenas F, Bouchard R. Stress-Strain-strain rate relation for the compressibility of sensitive natural clays. *Geotechnique* 1985;35(2):159–80.
- [43] Graham J, Crooks JHA, Bell AL. Time effects on the stress strain behaviour of soft natural clays. *Geotechnique* 1983;33(3):327–40.
- [44] Leroueil S, Marques MES. Importance of strain rate and temperature effects in geotechnical engineering. In: *Session on measuring and modeling time dependent soil behavior, ASCE Convention, Geotechnical Special Publication 61, Washington; 1996*.
- [45] Lefebvre G, LeBoeuf D. Rate Effects and cyclic loading of sensitive clays. *J Geotech Eng* 1987;113(5):476–89.
- [46] Einav I, Randolph MF. Combining upper bound and strain path methods for evaluating penetration resistance. *Int J Numer Meth Eng* 2005;63:1991–2016.
- [47] Biscontin G, Pestana JM. Influence of peripheral velocity on van shear strength of an artificial clay. *Geotech Test J* 2001;24(4):423–9.
- [48] Peuchen J, Mayne P. Rate effects in vane shear testing. In: *Proceeding of the 6th international offshore site investigation and geotechnics conference: confronting new challenges and sharing knowledge, London, UK; 2007*.
- [49] Jeong SW, Leroueil S, Locat J. Applicability of power law for describing the rheology of soils of different origins and characteristics. *Can Geotech J* 2009;46(9):1011–23.
- [50] Boukpeti N, White DJ, Randolph MF, Low HE. Strength of fined-grained soils at the solid-fluid transition. *Geotechnique* 2012;62(3):213–26.
- [51] Boukpeti N, White DJ, Randolph MF. “Strength of a carbonate silt at the solid-fluid transition and submarine landslide run-out”. *Frontiers in Offshore Geotechnics III - Meyer (Ed)*. 2015.
- [52] Sorensen KK, Baudet BA, Simpson B. Influence of strain rate and acceleration on the behaviour of reconstituted clays at small strains. *Geotechnique* 2010;60(10):751–63.
- [53] Hazell E. Numerical and Experimental studies of shallow cone penetration in clay. UK: Thesis at the University of Oxford; 2008.
- [54] Quinn T. Rate effects in fine grained soils PhD thesis at University of Dundee; 2013.
- [55] Chung SF, Randolph MF, Schneider JA. Effect of penetration rate on penetrometer resistance in clay. *J Geotech Geoenviron Eng, ASCE* 2006;63(14):1188–96.
- [56] Rattley MJ, Richards DJ, Lehane BM. Uplift performance of transmission tower foundations embedded in clay. *J Geotech Geoenviron Eng* 2008;134(4):531–40.
- [57] Moavenian M, Nazem M, Carter J, Randolph M. Numerical analysis of penetrometers free-falling into soil with shear strength increasing linearly with depth. *Comput Geotech* 2016;72:57–66.
- [58] Bardenhagen SG, Guilkey JE, Roessig KM, Brackbill JU, Witzel WM, Foster JC. An improved contact algorithm for the material point method and application to stress propagation in granular material. *Comput Model Eng Sci* 2001;1:509–22.
- [59] Mast CM, Mackenzie-Helnwein P, Arduino P, Miller GR, Shin W. Mitigating kinematic locking in the material point method. *J Comput Phys* 2012;231(16):5351–73.
- [60] Coombs WM, Charlton TJ, Cortis M, Augarde CE. Overcoming volumetric locking in material point method. *Comput Methods Appl Mech Eng* 2018;333(1):1–21.
- [61] Hungr O, Leroueil S, Picarelli L. The Varnes classification of landslide types, an update. *Landslides* 2014;11:167–94.
- [62] Bernander S. “Progressive landslides in long natural slopes, formation, potential extension and configuration of finished slides in strain-softening soils”. Licentiate thesis, Department of Civil and Mining Engineering. Sweden: Lulea University of Technology, Lulea; 2000.
- [63] Bernander S. “Downhill progressive landslides in soft clays, triggering disturbance agents, slide propagation over horizontal or gently sloping ground, sensitivity related to geometry,” Department of Civil and Mining Engineering. Lulea, Sweden: Lulea University of Technology; 2008.
- [64] Bernander S, Kullingsjo A, Gylland A, Bengtsson P, Knutsson S, Pusch R, et al. Downhill progressive landslides in long natural slopes: triggering agents and landslide phases modeled with a finite difference method. *Can Geotech J* 2016;53:1565–82.
- [65] Dey R, Hawlader B, Phillips R, Soga K. Numerical modeling of combined effects of upward and downward propagation of shear bands on stability of slopes with sensitive clay. *Int J Numer Anal Meth Geomech* 2016;40(15):2076–99.
- [66] Locat A, Leroueil S, Demers D, Locat J, Ouehb L. Study of a lateral spread failure in an eastern Canada clay deposit in relation with progressive failure: the Saint-Barnabe Nord slide. In: *Proceedings of the 4th Canadian conference on geohazards: from causes to management, Quebec, Canada; 2008*.
- [67] Locat A, Leroueil S, Bernander S, Demers D, Jostad H, Ouehb L. Progressive failures in eastern Canadian and Scandinavian sensitive clays. *Can Geotech J* 2011;48(11):1696–712.
- [68] Locat A, Leroueil S, Fortin A, Demers D, Jostad H. The 1994 landslide at Saint-Monique, Quebec: geotechnical investigation and application of progressive failure analysis. *Can Geotech J* 2015;52:490–504.
- [69] Lefebvre G. Sensitive Clays of Eastern Canada: From Geology to Slope Stability. In: *Landslides in sensitive clays. Advances in natural and technological hazards research, vol 46; 2017*.
- [70] Yin ZY, Karstunen M, Chang CS, Koskinen M, Lojander M. Modeling time-dependent behaviour of soft sensitive clay. *J Geotech Geoenviron Eng* 2011;137(11):1103–13.
- [71] Pinyol NM, Alvarado M, Alonso EE, Zabala F. Thermal effects in landslide mobility. *Geotechnique* 2017:1–18.
- [72] Thakur V, Nordal S, Viggiani G, Charrier P. Shear bands in undrained plane strain compression of Norwegian quick clays. *Can Geotech J* 2018:45–66.
- [73] Handwerker AL, Rempel AW, Skarbek RM, Roering J, Hillel GE. Rate-weakening friction characterizes both slow sliding and catastrophic failure of landslides. *Proc Natl Acad Sci* 2016.